Manganese redox cycling drives the epitaxial growth of dolomite on metastable kutnahorite templates

Daniel A. Petrash[1,2], Astolfo Valero[2], Or M. Bialik[3,4], Yihang Fang[5], Maartje Hamers[6], Travis B. Meador[2,7], Tomaso R.R. Bontognali[8,9,10] Michael Ernst Böttcher[11,12,13] and Oliver Plümper[6,14]

[1] Czech Geological Survey, Prague, Czech Republic, daniel.petras@geology.cz

[2] Biology Centre of the Czech Academy of Sciences, Czech Republic

[3] University of Münster, Germany

[4] Israel Oceanographic and Limnological Research, Israel

[5] University of Missouri–Kansas City, USA

[6] Utrecht University, The Netherlands

[7] University of South Bohemia, Ceske Budejovice, Czech Republic

[8] Space Exploration Institute, Switzerland

[9] University of Basel, Switzerland

[10] Environmental Science Centre, Qatar, Qatar

[11] University of Greifswald, Germany

[12] University of Rostock, Germany

[13] Leibniz Institute for Baltic Sea Research, Germany

[14] University of Bremen, Germany

Abstract

Fine-crystalline, fabric-preserving dolostones in deep-time successions defy high-temperature burial models, implying an elusive low-temperature formation pathway hindered by the kinetic hydration barrier of Mg^{2+} and the thermodynamic miscibility gap separating calcite from ordered dolomite. Here, we demonstrate a kinetically facile route to self-assembling dolomite driven by the synergy of manganese redox cycling and carboxyl functionalization. Using a bio-inspired electrochemical reactor, we show that electrochemical valence-state modulation selectively regulates Mn^{2+} co-precipitation. Unlike inorganic controls where manganese is rapidly sequestered into non-templating phases, the functionalized system stabilizes reactive Mn(III) intermediates. This sustained redox cycling prevents irreversible oxide immobilization and templates the rapid nucleation of spheroidal magnesian-kutnohorite. Nanostructural characterization reveals a core-shell architecture where this metastable, isostructural precursor serves as a lattice-distorted scaffold, enabling the heteroepitaxial growth of substitutionally disordered dolomite cortices. Mechanistically, localized acidity from redox cycling triggers a "proton-driven cation pump," actively liberating Mg^{2+} from the functionalized hydrogel reservoir to the mineralization front. This electrochemical mechanism offers a unifying geological model that links the massive fabric-retentive dolostones of the Precambrian to ancient Mn-stratified oceans, while explaining the Phanerozoic scarcity of dolomite as a consequence of global oxygenation decoupling the manganese redox shuttle from shallow marine environments.

1. Introduction

The massive accumulation of fabric-retentive, fine-crystalline dolostones in the geological record—most notably in the Precambrian but also in specific Phanerozoic intervals like the Triassic—implies a low-temperature formation pathway mechanistically distinct from the burial diagenetic models often applied to replacive coarse-crystalline dolostones (Hood et al.,

2011, Bontognali, 2019; Chang et al., 2020). While the kinetic inhibition exerted by Mg^{2+} hydration is well-established (Lippmann, 1973), direct dolomite nucleation is further hindered by the miscibility gap separating the stability fields of calcite and the ordered dolomite-group carbonates (Goldsmith and Graf, 1960). Direct nucleation of these ordered phases requires traversing this thermodynamic discontinuity, where metastable Ca-rich phases are structurally distinct from the final double-carbonate product.

To bridge this gap, we propose a redox-driven solution to the long-standing "dolomite problem." We hypothesize that the primary driver for syndepositional dolomite is an active manganese redox engine. Unlike the Ca-Mg system, the Ca-Mg-Mn system offers a continuous solid solution series (Goldsmith and Graf, 1960). Specifically, redox oscillations can drive the nucleation of metastable kutnahorite (Mucci, 1988; Peacor et al., 1987). This phase acts as a distorted nanocrystalline scaffold, where the larger Mn^{2+} radius expands the lattice, significantly lowering the activation energy for subsequent Mg^{2+} incorporation and driving the chemical evolution of the lattice across the miscibility gap (Han et al., 2024). This recursive process drives a continuous out-of-equilibrium precipitation mechanism that ultimately leads to the neomorphism of the metastable, isostructural precursor into dolomite.

Here, we validate this hypothesis using a bio-inspired electrochemical reactor that mimics the redox-stratified interfaces of ancient microbial mats, where redox-reactive Mn accumulates (Petrash et al., 2015). We demonstrate that inducing quasi-reversible Mn(II)↔Mn(III) redox cycles on carboxyl-functionalized surfaces enhances Mg incorporation relative to passive controls. Mechanistically, this enhancement effect functions as a proton-driven cation pump. Localized acidification driven by Mn(II) oxidation "depins" Mg^{2+} and Ca^{2+} complexed in the hydrogel, concentrating them at the mineralization front. This active mobilization, buffered by proton-consuming Mn-reduction cycles, drives the rapid nucleation of spheroidal magnesian-kutnahorite as metastable precursor, which serves

as an epitaxial scaffold, lowering the kinetic barrier for the subsequent crystallization of disordered dolomite.

This electrochemical mechanism provides a framework for explaining the paragenesis of delicate, fabric-retentive dolostones observed throughout the rock record. We propose that this coupling, linking manganese availability to precursor dolomite precipitation, was a fundamental driver for the massive, basin-wide fabric retentive dolomicrite facies characteristic of the Precambrian. By identifying this catalytic engine, we can also explain the distribution of massive dolomite in the Phanerozoic sedimentary rock record as a consequence of the spatial (de)coupling of manganese redox cycling from shallow carbonate platforms.

2. Methods

2.1 Precipitation setup

The experimental design comprises a H-cell electrochemical system (150 mL borosilicate glass reaction vessels) connected to an automatic titrator (SI Analytics Titroline 7000). The electrochemical system was filled with 125 mL of 80 mM $NaHCO_3$ electrolyte solution and it cells were separated by an anion exchange membrane (Fumasep® FKE-50, Fumatech GmbH); and were continuously stirred at 250 rpm via synchronized MIXDrive stirrers (2Mag). One cell was open through a 0.2 µm cellulose acetate filter to maintain the dissolved inorganic carbon of our electrolyte in equilibrium with the atmosphere at 25°C. The headspace of the other cell was kept anoxic by a constant flow of argon, initiated 5 min before experiments. In the anoxic cell, a graphite rod working electrode (WE, CP-2200, CP-Graphitprodukte GmbH) and an Ag/AgCl reference electrode (sat. KCl, +197 mV *vs.* standard hydrogen electrode (SHE); RE-1B, ALS Japan) were inserted. In the oxic cell, another graphite rod was used as the counter

electrode (CE). A schematic representation of the electrochemical system is shown in Figure 1.

To investigate the influence of carboxyl functionalization, to a set of experiments we added to the electrolyte Na-alginate (300 $mg \cdot L^{-1}$, Sigma-Aldrich)—a commercially available compound composed exclusively of carboxyl functional groups. Alginate, a carboxyl biomolecule, is key component of EPS in microbial mats colonizing hypersaline, dolomite-forming settings (Bontognali et al., 2010). At the environmentally relevant pH range (i.e., >p*K*a) alginate is crosslinked by metal ions, forming a hydrogel (Petrash et al., 2011). This property can render the resulting hydrogels conductive (e.g., Ji et al., 2022).

To isolate the effects of organic functionalization and electrochemical modulation on mineral formation, four experimental conditions were tested: **(E_{00})** control, lacking both functionalization and electrochemical modulation, served as the baseline for surface precipitation; **(E_{10})** carboxyl-functionalized without electrochemistry, this condition isolated the effect of the carboxyl groups on mineral formation in the absence of an applied potential; **(E_{01})** a non-carboxyl-functionalized sample was subjected to electrochemical modulation to assess the role of redox cycling in the absence of the biopolymer; **(E_{11})** a carboxyl-functionalized surface with an applied electrochemical treatment to evaluate potential synergistic or antagonistic interactions. All conditions were conducted in duplicate.

2.2 Electrochemical precipitation protocol

During each experimental run, an initial pH value of 8.5 ± 0.1 in the anodic cell was raised to 9.1 units after additions of 100 to 200 µL of 0.5 M NaOH solution as pre-titrant. Following pre-titration, a cation-rich feedstock (0.6 M $(Ca,Mg)Cl_2$; Mg:Ca = 6:1) was dosed into the anodic chamber at a rate of 1 mL min^{-1} for 20 minutes (20 mL total); the final working volume of the H-cell setup was 145 mL. The electrolyte pH was maintained at 9.2 ± 0.4 by

automatically dosing the titrant into the anodic cell (1.2 to 3.0 mL in total) using the automatic titrator in pH-stat mode. when the value dropped below the experimental pH-envelope.

After the first 5 min of feedstock dosing (*ca*. 5 mL), a single addition of $MnCl_2$ stock solution was added to the anodic cell to achieve a concentration of 10 mM Mn. At this nucleation onset (t = 5 min), the system had reached estimated concentrations of Mg ≈ 21 mM and Ca ≈ 3.6 mM. This established a far-from-equilibrium state—supersaturated with respect to Mg-Ca phases but undersaturated for Mn-precursors (Table S1)—effectively isolating Mn-nucleation to the electrode interface. As feedstock dosing continued to completion (t = 20 min), the background concentrations rose to Mg ≈ 86 mM and Ca ≈ 14 mM, sustaining the high thermodynamic driving force. Deionized water (18.2 $M\Omega \cdot cm^{-1}$) and analytical-grade reagents were used to prepare all solutions. Concurrently with reactant dosing, oscillations in the redox potential of the electrolyte were induced by using a Dropsens μStat 8000 multichannel potentiostat (Metrohm, Spain) in cyclic voltammetry mode (CV) for 28 min. The electric potential was continuously swept between -0.1 and 0.5 V at a scan rate of 2 mV s^{-1}. This environmentally relevant Eh window (e.g., Jørgensen et al., 1979; Di Loreto et al., 2021) targets the Mn(II)/Mn(III) couple, driving oxidative cycling at the periphery of the working electrode (WE) without inducing water hydrolysis or insoluble Mn(IV) oxide precipitation. It aligns with the nitrogenous and manganous zone where incomplete manganese cycling is thermodynamically dominant (Petrash et al., 2025). After titration, the electrolyte solution in the anodic cell was left undisturbed for 24 h to permit stabilization of the surface precipitates. Following this step, the WEs were retrieved, disassembled, and stored under anoxic conditions until solid-phase characterization.

2.3 Solution cation concentration determinations

Samples were collected from the anodic chamber at three distinct experimental stages: **(S_i)** immediately before the addition of 10 mM $MnCl_2$—when 5 mL of the $(CaMg)Cl_2$ reactant

(further referred here to as cation feedstock) had been added (i.e., $[Ca]_{added}$ = 3.6mM, $[Mg]_{added}$ = 21mM; Mn = 10 mM); **(S_{ii})** following the complete dosing of 20 mL of the cation feedstock (i.e., $[Ca]_{added}$ = 14mM, $[Mg]_{added}$ = 86 mM, $[Mn]_{added}$ = 10mM); and **(S_{iii})** after the 24 h stabilization period. The working solutions were acidified with trace grade HNO_3 (67% v/v, Sigma-Aldrich). The cations crosslinking alginate are recovered after acidification, and the concentrations of Ca^{2+}, Mg^{2+}, and Mn^{2+} relative to the total analyte added to the system are determined using a triple quadrupole inductively coupled plasma mass spectrometer (ICP-MS; Agilent 8800). Precision was verified against certified standards, and the relative standard deviation was <10% of the reported value for all measurements.

2.4 Multiscale microscopy and nanoscale characterization

Electron-transparent lamellae of surface precipitates were prepared for (scanning) transmission electron microscopy ((S)TEM) using a Helios Nanolab G3 (Thermo Fisher Scientific) focused ion beam scanning electron microscope (FIB-SEM) at the University of Utrecht. This instrument was also employed to assess the micrometre-scale morphological features of the precipitates. Sub-micron scale imaging of lamellae, with thicknesses ranging from 250 to 300 nm, was conducted in bright-field (BF) TEM, dark-field (DF) TEM-EDS, and high-angle annular dark field (HAADF) STEM modes. These were performed using either a Thermo Fisher Talos F200X coupled to a Super-X detection system, or a Spectra 300 instrument, operated at accelerating voltages of 200 kV and 300 kV, respectively. Selected area electron diffraction (SAED) and electron energy loss spectroscopy (EELS) were further utilized in multiple regions of interest to resolve crystallographic and compositional features of the precipitates at the nanoscale. Dual-EELS datasets (core- and low-loss regimes) were acquired using a CCD camera and DigiScan within the Gatan microscopy suite, with a dispersion of 0.15 eV/pixel and a convergence angle of 0 mrad. The low loss spectrum was used to align the core region and evaluate the lamella thickness. To estimate the manganese valence state, we

176 employed a combined approach: semi-quantitative background-subtracted white line intensity
177 ratios (L_3/L_2) and the deep-learning spectral decomposition framework MnEdgeNet (Ji et al.,
178 2023). For the latter, spectra were analyzed using the noise-free model to strictly constrain
179 oxidation states based on peak position and spectral shape. Additionally, energy-dispersive X-
180 ray spectroscopy (EDS) was employed to map the spatial distribution of Mn, Ca, and Mg within
181 sacrificial areas of the precipitates.

182 **3. Results**

183 **3.1 Response to titration and electrochemical treatments**

184 Titration data (Fig. 2) show that control samples (E_{00}) required maximal external neutralization
185 due to unbuffered proton release during precipitation. Conversely, potential sweeping alone
186 (E_{01}) reduced titrant demand via cathodic proton consumption (Eq. 1). Conversely, potential
187 sweeping alone (E_{01}) reduced titrant demand via cathodic proton consumption (Eq. 1). In E_{01},
188 proton-coupled electron transfer partially offsets the release associated with carbonate
189 precipitation, explaining the reduced external titrant demand observed in the electrochemical
190 condition.

191 $$Mn^{III}(OH)_{org} + e^- + H+ \rightarrow Mn^{II}_{org} + H_2O \quad (1).$$

192 The carboxyl functionalization alone (E_{10}) provided intrinsic buffering capacity,
193 attributed to carboxyl groups (pKa ~3.5–4.5; e.g., Petrash et al., 2011). At the experimental
194 pH, the carboxyl-rich biopolymer forms a hydrogel upon deprotonation and in the presence of
195 cations. As carbonate mineral nucleates, it pulls CO_3^{2-} from the equilibrium, forcing the
196 deprotonation of HCO_3^-. This locally weakens the bond between metals, M, cross-linking the
197 hydrogel as the crystal growth front, releasing these metals back in solution right at the interface
198 of the growing mineral phase (2).

199 $$R\text{-}COO\text{-}M\text{-}OOC\text{-}R + H^+ \rightarrow R\text{-}COOH + M^{2+} + {}^-OOC\text{-}R \quad (2).$$

The combined system (E_{11}) achieved maximal pH buffering capacity by synergizing active cathodic reduction with passive hydrogel buffering. This dual mechanism effectively mitigated the acidification front driven by rapid carbonate nucleation, resulting in minimal titrant consumption during cation feedstock addition (Fig. 2)

3.2 Mn redox features developed during electrochemical carbonate synthesis

CV was used to investigate the electrochemical behavior of Mn in the system. In experiments lacking Na-alginate, the graphite electrode showed negligible faradaic activity within the potential window (-0.1 V to +0.5 V vs. SHE), displaying a non-faradaic capacitive current profile (Fig. 3A). Upon the introduction of Na-alginate, distinct quasi-reversible redox features emerged (Fig. 3B). Accordingly, an anodic peak attributed to the oxidation of Mn(II) → Mn(III) was observed at approximately +0.35 to +0.45 V, with a corresponding cathodic peak for the reduction reaction appearing at ca. +0.30 V during the reverse scan (Fig. 3B). This quasi-reversibility indicates that carboxyl functionalization does not merely lower the activation energy but enables the electrochemical reaction. By acting as inner-sphere ligands, the carboxyl groups near the surface of WEs could facilitate electron transfer that is otherwise kinetically inhibited at the bare graphite interface. Therefore, the presence of the return (cathodic) peak confirms that the surface ligand field stabilizes the highly reactive Mn(III) intermediate.

To also monitor the progression of the surface-mediated reaction in functionalized experiments, we recorded the temporal evolution of the current response. The system exhibited reproducible periodic current oscillations, where each 4'-cycle (corresponding to a full potential sweep) featuring sharp anodic and cathodic spikes (Fig. 3C). The pattern confirms the sustained cyclic oxidation and reduction of manganese bound to the carboxylated hydrogel during the active synthesis stage. The signal intensity displayed a progressive attenuation over time (Fig. 3C), indicating that the electroactive surface area was being systematically

passivated by deposition of carbonate on the surface of the electrode, leading to fouling and decreased anodic and cathodic capacity.

3.3. Aqueous composition of the reactive solutions

3.3.1. Magnesium removal: kinetic enhancement

The bulk of Mg removal initiated after 5 doses of the cation feedstock and the single Mn addition. Therefore, S_i recorded [Mg] below certainty levels. By the end of the reactant dosing and titration stage (S_{ii}), between 8.7 ± 1.1% to 28.0 ± 1.0% Mg^{2+} has been removed from solution; enhanced by the electrochemical treatment (Fig 4A). Removal, however, remained incomplete even after the stabilization time lag (S_{iii}), with 66% to 87% of the total Mg^{2+} added to the system persisting in solution across the disparate conditions tested. Electrochemistry alone (E_{01}) achieved the highest removal rates, surpassing the control (E_{00}) by approximately 20%. Electrochemistry with functionalization (E_{11}) was also effective. However, the total amount of Mg co-precipitated in E_{11} was lower than in the functionalized-only condition (E_{10}). Subsequent removal during stabilization was sluggish, increasing by only 3% to 6% relative to the amount removed by the end of titration (Fig. 4A; Table 1).

3.3.2. Calcium removal: Calcium availability as a rate-limiting factor

Prior to the addition of Mn (S_i), approximately 40% of the total Ca had already been removed from the solution (Fig. 4B). This initial depletion is attributed to a quasi-instantaneous homogeneous nucleation of fine-grained suspended precipitate formed upon dosing the cation-rich feedstock into the electrolyte. Similar rapidly formed metastable phases have been characterized as amorphous (e.g., Purgstaller et al., 2016). Considering our Mg^{2+} removal trends via co-precipitation (Fig. 4A), and the extremely low Mg-distribution coefficient between amorphous calcium carbonates (ACC) and the mother solution (Purgstaller et al., 2019), we deduce that the bulk of this solid residue may be initially an ACC precursor that

249 actively rejected Mg^{2+} during exsolution. Consistent with this assertion, XRD analysis of the
250 residual solids from experiment E_{11} identifies them as aragonite associated with secondary
251 hydrated Mg-carbonate, dypingite (Fig. S1). This assemblage directly reflects the bulk
252 saturation state of the residual solution, S_{iii} (SI_{Arag} = 2.41 and SI_{Hmag} = 5.01; Table S1). The
253 result is consistent with solid-state transformation of the initial ACC that segregated into
254 distinct Ca and hydrated-Mg phases upon aging and dehydration of S_{iii} at ambient temperature.

255 During the active synthesis stage (S_{ii}), Ca removal continued, reaching between 65–
256 84% across all experiments. Following stabilization (S_{iii}), most conditions exceeded 95%
257 removal, except for the functionalized, and electrochemically active experiment (E_{11}, ~75%),
258 where ligand complexation and interfacial electrochemical dynamics rendered it unavailable
259 for co-precipitation (Fig. 4B; Table 1).

260 *3.3.3. Manganese removal: Redox-driven sequestration*

261 Mn removal exhibited a distinct, redox-driven pattern compared to Mg. After 20 doses of the
262 Mg-Ca reactant (S_{ii}), removal of Mn varied across experimental conditions, and showed the
263 strongest kinetic response to electrochemical treatment. Accordingly, Mn removal ranged from
264 10.2 ± 7.2% to 61.4 ± 17.3%, with electrochemical sweeping without functionalization (E_{01})
265 yielding the highest scavenging efficiency, far exceeding both the only functionalized
266 experiment (E_{10}) and the control (E_{00}). Remarkably, after the 24 h equilibration (S_{iii}), Mn
267 depletion approached >99% in most conditions, indicating near-complete incorporation into
268 the solid phases. The significant exception occurred in E_{11} (electrochemical + functionalized),
269 where 25–38% of the total Mn remained in solution. This indicates that while the potential
270 sweep drives oxidation-reduction, some of the carboxyl ligands in E_{11} can stabilize a significant
271 fraction of the Mn ions available in the system (see Tordi et al., 2025), thus preventing the
272 almost complete sequestration observed in non-functionalized controls (Fig. 4C; Table 1).

3.4 Mineralogical and textural characterization of precipitates

Neither electrochemical cycling nor functionalization alone produced dolomite-composition-like phases. Controls (E_{00}) yielded only minimal, sparse Mn-rich precipitates on the WE (Fig. 5A). Functionalization without electrochemistry (E_{10}) increased precipitate density, forming manganous Mg-Ca carbonate spheroids (Fig. 5B–C). TEM in various modes (Fig 5D-F) showed that the crystallites comprising these fabrics grow outward from central nucleation points, forming spherulitic structures with radially arranged crystallites.

Electrochemical cycling without functionalization (E_{01}) yielded disperse aggregates resulting from the rapid coalescence (self-assembly) of multiple nanocrystalline domains. In these experiments, a Mg-carbonate phase forming rosettes was observed (Fig. 6A). The delicate texture—likely a hydrous phase—was unstable under the ion beam and could not be recovered during FIB-lamella preparation (Fig. 6B). STEM-HAADF imaging reveals that the recovered aggregates exhibited significant internal porosity ("hollow"), consistent with self-assembly during growth (Fig. 6C). Chemically, these aggregates display a magnesian-calcian rhodochrosite composition. It displays distinct zoning indicated by Z-contrast gradients portraying denser Mn-enriched domains transitioning into Ca-Mg enriched inner domains, and with Mg homogenously distributed along the aggregate rims (Fig. 6C–E). SAED ring assignments generated a d_{104} spacing of ~2.84 Å, alongside d_{113} (2.39 Å) and d_{110} (2.16 Å) reflections (Fig. 6F).

Condition E_{11} yielded dense carbonate coatings consisting of 1–3 μm polycrystalline spheroidal aggregates (Fig. 7A–C). Internally, these aggregates are defined by the coalescence of smaller (200–600 nm) spheroids with Mn-enriched, thread-like cores and variably Mg-enriched cortices (Fig. 7C–D). TEM-EDS confirms preferential Mn partitioning in the cores, with oscillatory zoning likely induced by potential swapping (Fig. 7E). To resolve the potential for solid solution extending to the dolomite-kutnahorite series (*cf.* Peacor et al., 1987), we

plotted the EDS data on a ternary Ca-Mg-Mn diagram (Fig. 7H). The data reveal a continuous kinetic trajectory where metastable magnesian-calcian rhodochrosite, formed in the cores, transitioned into manganoan protodolomite cortices. Notably, these intermediate compositions plot directly within the thermodynamic miscibility gap defined by Peacor et al. (1987), indicating that rapid kinetic growth stabilized a continuous solid solution that reflects disequilibrium crystallization. In contrast, the E_{01} as magnesian- rhodochrosite products cluster distinctly at the magnesite- calcian rhodochrosite solvus (Fig. 7H); i.e., the E_{01} phase is presumably stable.

Structurally, HR-TEM reveals that our two-phase manganoan carbonate spheroids posses a mosaic texture composed of nanodomains separated by broad, diffuse low-angle boundaries (Fig. 7F). FFT analysis (Fig. S3) confirms crystallographic misorientations (3–11°) between these regions. Diffraction rings in the SAED patterns (Fig. 7G) confirm that E_{11} yielded a polycrystalline, randomly oriented precipitate. Overall, the measured interplanar distances of the cores are consistent with disordered kutnahorite, while the cortices exhibit reflections consistent with a disordered dolomite with near-stoichiometric cation ratio (i.e., Ca : (Mg + Mn) = 1) as per d_{104} *ca*. 2.88 Å. Other reflections that can confidently assigned are d_{101} (4.029 Å), d_{110} (2.404 Å), d_{113} (2.191 Å), and d_{116} (1.786 Å). The characteristic b-type superstructure reflections (e.g., d_{015}, d_{021}, etc), which signify cation ordering, were unresolved.

3.5 EELS of the cortical precipitates

The results from EELS targeting the synthetic products from E_{11} are shown in Figure 8A-D. The carbon K-edge spectra are characterized by sharp pre-edge peaks at 290.4 eV and broader features at 300.9 eV, corresponding to the π* and σ* resonances of the C=O bond, respectively. These transitions combined with corresponding O *K*-edges at ~531 eV, uniquely identify the matrix as carbonate (Fig. 8A-B). The Ca $L_{3,2}$-edge (Fig. 8C) shows well-resolved spin-orbit splitting (L_3 at 349 eV), confirming the integration of Ca into a crystal lattice. Most

significantly, the spectra capture characteristic Mn $L_{3,2}$-edge features in the 640 to 650 eV range (Fig. 8D). Mn $L_{2,3}$ edge spectra ($N = 4$) from the core of a representative spheroid were analyzed using the deep-learning framework MnEdgeNet (Ji et al., 2023). The Supplementary Data 1 (Fig. S4) contains the MnEdgeNet modelling results. The combined data exhibit L_3/L_2 white line intensity ratio ≈ 2.88 with an L_3 absorption maximum located at 639.5–640.0 eV. The applied MnPredictor decomposition was the 'noise-free' model, which prioritizes peak position fidelity and spectral shape. It returned to an average oxidation state (AOS) of +2.03, indicating ≥98.6% Mn(II) (Fig. 8D). This predominantly divalent state is physically confirmed by the deep spectral valley between the L_3 and L_2 edges (arrow in Fig. 8D), which reaches baseline intensity.

4. Discussion

We presented an electrochemical synthetic pathway that circumvents the kinetic barriers inhibiting the incorporation of the Mg^{2+} ion in dolomite by leveraging the redox chemistry of Mn on reactive functionalized surfaces. This result establishes a mechanistic link between dolomite and manganese redox-cycling (Petrash et al, 2015), organic functionalization and ionic lattice distortion (Han et al., 2024), and links the increasingly recognized role of electron transfer mechanisms in marine sediments (Nielsen et al., 2010).

Cyclic voltammetry demonstrates that carboxyl functionalization modulates the electrochemical behavior of manganese, facilitating quasi-reversible Mn(II) ↔Mn(III) valence state transitions that are otherwise kinetically inhibited at the WE interface. Our central finding is the formation of compositionally zoned spheroids, which featured Ca-Mn-enriched cores and Mg-enriched cortices. The discussion below expands on observations, their interpretations and implications.

4.1 The Mn-templating mechanism

Morphological and nanostructural characterization reveals that low-temperature formation proceeds via a non-classical, multi-stage pathway involving metastable precursors. In the solid-phase products of E_{11}, STEM-HAADF imaging, SAED, and EDS mapping identify Mn-rich cores with minor Mg incorporation. These cores serve as epitaxial templates for the subsequent overgrowth of a Mg-enriched cortex—a compositional evolution significantly promoted by carboxyl functionalization and potential modulation. The composite E_{11} spheroids have cores analogous to "pseudo-kutnahorite" (Mucci, 1988), and cortices that are consistent with a manganoan (proto)dolomite precursor—given the absece of ordering reflections.

It is worth noticing, however, that the absence of ordering reflections may be a methodological artifact rather than intrinsic disorder of the products. Relative thickness mapping ($t(\lambda)^{-1}$) derived from the low-loss EELS spectrum reveals that the dolomitic cortices correspond to the thinner regions of the lamellae yet these exhibit local $t(\lambda)^{-1}$values ranging from 0.86 to 0.88 (Fig. S5). In this regime, approximately 59-64% of the incident electrons undergo inelastic scattering (Egerton, 2011). This substantial background contribution, combined with the polycrystalline nature of our synthetic products, likely lowers the signal-to-noise ratio sufficiently to obscure weak superlattice reflections possibly associated with incipient cation ordering. Consequently, while the current SAED data are consistent with a disordered precursor, the sample thickness was not optimal for definitively resolving any faint b-type reflections characteristic of substantial Ca occupancy in the B site. Attenuation of b-type reflections may also be from manganese occupying a substantial portion of the magnesium sites within this disordered lattice structure (Peacor et al, 1987).

Although kutnahorite is metastable at near-surface temperatures (Peacor et al., 1987; Mucci, 2004; Böttcher and Dietzel, 2010), our results show that formation of this phase is kinetically favored over disordered dolomite under functionalized conditions. While

thermodynamics alone dictates that dolomite is the more stable phase ($\Delta G^{o}_{f\_dol} < \Delta^{o}_{f\_Kutn}$; Rosenberg and Foit, 1979), kinetic factors—specifically those governing the descent of the free energy landscape, ultimately influence the reaction pathway. In this regard, despite the bulk electrolyte being undersaturated with respect to kutnahorite (SI = -2.57; Table S1), the out-of-equilibrium experiments implemented here indicate that this precursor presents a significantly lower activation energy barrier to nucleation than direct precipitation of oversaturated dolomite (SI = 5.54). This advantage is probably rooted in coordination chemistry as Mn^{2+} has a lower magnitude of dehydration enthalpy compared to Mg^{2+} (-1851 vs. -1926 kJ mol^{-1}; Marcus, 1987), and its water exchange rate is nearly two orders of magnitude faster (2.1 10^{7} s^{-1} *vs*. 6.7 10^{5} s^{-1}; Helm and Merbach, 2005). This allows Mn^{2+} ions to desolvate and occupy the carbonate lattice rapidly, effectively bypassing the barrier that stalls Mg incorporation.

Other factors may also be at play. The high lattice strain inherent to dolomite (determined by its cationic mismatch ratio, R_{Ca}/R_{Mg} ~ 1.38) may contribute substantially to the energetic barrier inhibiting its formation at low temperature. In contrast, within the octahedral geometry, Mn^{2+} possesses an effective ionic radius ~15% larger than that of $Mg2^{+}$ (0.83 Å *vs*. 0.72 Å). This yields a significantly lower mismatch ratio for kutnahorite (R_{Ca}/R_{Mn} ~ 1.20) and places the latter phase within a (meta)stability window where lattice strain is sufficiently low to avoid the kinetic penalties that prevent dolomite nucleation/growth. However, lattice-ordering in multicomponent phases is governed by factors beyond simple cation radii (Jakob et al., 2025). In our system, cation-partitioning can also be critical. Mucci (1988) and Böttcher (1998) demonstrated that the Mg distribution coefficient (D_{Mg} is notably higher in Mn-bearing environments. As the [Mg]/([Mn]+[Ca]) ratio progressively rises during precipitation, D_{Mg} increases, facilitating the incorporation of Mg^{2+} into the Mn-expanded lattice of the kutnahoritic precursor. Being manganoan, this phase—exhibiting a

small lattice mismatch (<1.5%; a_{Kut} = 4.8732(8) Å, a_{Dol} = 4.8012(1) Å), still has some degree of structural distortion (Rosenberg and Foit, 1979).

HRTEM imaging of E_{11} synthetic products reveals that they consist of aggregated nanocrystals with incoherent orientations, possibly implying formation through an assembly of nanoparticle subunits sharing a common crystallographic motif (Cölfen and Mann, 2003). Such variations can force the coexistence of regions with disparate unit cell parameters that may locally exhibit higher-order superstructures (Fang and Xu, 2019; Meister et al., 2023). Forming as the crystal progresses towards a Mg-Ca stoichiometry that is thermodynamically closer to equilibrium, the nanoscale misorientations accommodate lattice misfit (Van Tendeloo et al., 1985). These circumvent the „step-pinning barrier“ by stabilizing the strained surface, thereby preventing rapid monolayer dissolution inherent to slow Mg-dehydration (Higgins and Hu, 2005). In the absence of such a favourable isostructural template, the slow dehydration of magnesium typically leads to strained initial surface layers that undergo rapid monolayer dissolution before stable critical nuclei can grow. Our results demonstrate that the isostructural Mn-rich core stabilizes these initial layers, preventing dissolution and enabling the heteroepitaxial growth of the disordered dolomite cortices on kutnahoritic cores.

4.2 Carboxyl biomolecules and redox potential oscillations

The nucleation mechanism is governed by the synergy between organic functionalization and the applied potential sweep. This mimics the interfacial processes active at the reactive surface of sedimentary Mn-bearing phases that can be present in chemically stratified dolomite-precipitating depositional systems (e.g., Petrash et al., 2015). The carboxyl acts not merely as a passive template, but as an active agent that modulates, in its interaction with reactive Mn, the free energy landscape, driving the distinct morphological and mineralogical outcomes (Mercedes-Martín et al. 2016).

The interplay between the polymeric matrix and the electric field dictates the growth habit. In the passive functionalized condition (E_{10}), precipitation follows a radial, isotropic pathway. The presence of the biopolymer drives supersaturation and nucleation near the WE surface occur stochastically from the initial seed. As described by Gránásy et al. (2005), such 'non-crystallographic branching disrupts the crystalline anisotropy early in the growth process, leading to isotropic spherulitic growth.

In contrast, the synergy of carboxyl functionalization and electrochemistry in E_{11} shifts the system toward the Category 2 growth mode of Gránásy et al. (2005), shifting the reaction profile from themodynamic to kinetic driving forces (Cölfen and Mann, 2003). In this condition, the polarized alginate chains likely establish a directional electric field along the hydrogel, initially inducing a fibrillar habit by stabilizing metal ions via oriented attachement (De Yoreo et al., 2015). However, the defining driver is the evolution of supersaturation near the electrode interface. As the growing crystal entered a compositional zone where lattice strain blocked classical step-flow mechanisms, the interfacial fluid built up extreme supersaturation. To bypass this kinetic barrier, the crystal is forced to grow by rapidly incorporating Mg-rich nanoparticle arrays that may result in oscillatory zoning. This mechanism explains the continuous trajectory observed in the ternary plot (Fig. 7H), as rapid kinetic attachment in an increasingly Mg-rich solution increasingly captures metastable phases, effectively bridging the miscibility gap as the composition converges upon the double-carbonate stability field.

4.2.1 The electrochemical "engine"

The reoxidation of aqueous Mn(II) requires an inner-sphere mechanism where water is displaced by anionic ligands (Luther, 2005). Alginate carboxyl groups serve this function, substituting for water molecules to enable electron transfer to the electroactive manganese reactant (Fig. 9A). As the local activity of Mn^{2+} is progressively decreased, these same

ligands transition to binding the increasingly abundant Mg^{2+} ions (Fig. 9B). This evolution in the mother solution is chemically coupled to the solid product via the pre-existing Mn-rich isostructural surface. Driven by ionic radius compatibility and the distribution coefficient (D_{Mg}) covariation (Mucci, 1988; Böttcher, 1998), the initial kutnohoritic core can serve as a lattice bridge that facilitates heteroepitaxy.

This mechanism is fueled by localized interfacial acidification arising from two synergistic sources: (i) carbonate precipitation, and (ii) the stoichiometric proton release coupled to the incomplete anodic oxidation of Mn(II) (Fig. 3B). Estimates using a steady-state Nernst approximation suggest this anodic flux induces a local acidification (ΔpH ~ -0.5 to -1.2 units) within the diffusion boundary layer at the WE surface (see Note S1 in the Supplementary Data 1). This transiently protonates the carboxyl ligands (pK_a ~4), triggering the "depinning" of cross-linked cations, Mg^{2+}, Mn^{2+}, and Ca^{2+}, that become available for incorporation into growing cortices (Fig. 9B). Transient accumulation of H^+ near the reactive (WE) surface create oscillating supersaturation regimes required to stabilize pre-nucleation clusters (De Yoreo et al., 2015) and generate oscillatory zoning inthe overgrowths (e.g., Katsikopoulos et al., 2009).

Finally, carboxyl functionalization alters the thermodynamic fate of the intermediate Mn species. As delineated by the Eh-pH stability fields (Fig. S6), our experimental conditions (-0.1 to +0.4 V. pH_{surf} ±1.2 units) oscillate across the critical solubility threshold separating hausmannite (Mn_3O_4) and manganite (MnOOH). The absence of organic ligands, crossing this boundary, results in rapid Mn(III) disproportionation and irreversible precipitation (Luther, 2005). However, as evidenced by cyclic voltammetry (E_{01}), the organic ligand-free interface is kinetically inhibited, showing negligible faradaic activity. Substantial Mn removal observed in this experiment (Table 1) thus acts as a control for readily occurring, non-electrochemical Mn-carbonate precipitation. In contrast, functionalization in E_{11} enables

the quasi-reversible regeneration of Mn(III) in the system (Fig. 3), isolating a fraction of it from precipitation. This paradoxically results in lower net Mn removal (Table 1), confirming that the carboxyl ligand field induces kinetic stabilization of Mn(III) in the hydrogel and progressive Mn(II) incorporation in carbonate. The ligands allow the electrode to reductively cycle Mn(III), sustaining the redox engine (Fig. 9A-B), while avoiding the irreversible elctoractive reactant loss observed in E_{01}. Thus, the organic matrix (alginate) transforms the system from a passive chemical sink into an active electrochemical engine (Eq. 3):

$$[\text{R-COO-Mn}^{\text{III}}(\text{OH})] + e^- + H^+ \rightarrow [\text{R-COO-Mn}^{\text{II}}] + H_2O \quad (3)$$

4.3. Broader geo(bio)logical implications

4.3.1. Resolving the synsedimentary deep-time dolomite paradox

In this section, we interpret the manganese-rich bands frequently observed in ancient dolomite crystals not merely as diagenetic artifacts, but as a persistent chemo-textural fingerprint of Mn-catalysis (Petrash et al., 2021). We propose that this catalytic mechanism, by lowering the kinetic barrier for nucleation, acted as the fundamental driver that scaled up to produce the massive, basin-wide, fabric-retentive dolostone facies characteristic of the Precambrian. It likewise accounts for the cryptomicrobial dolomicrite facies that exhibit punctuated abundance in the Phanerozoic, such as those deposited in the Western Tethyan realm during the Triassic (e.g., Aljinović et al., 2025). With this crystal-to-facies link established, the lithostratigraphic and sedimentological metadata for the dolostone deposits considered in this section (listed in Note S2, Supplementary Data 1) can be understood as the macroscopic record of this chemical coupling. For this purpose, we examine the temporal correlation between massive dolostone intervals (Li et al., 2021, Shang, 2023) and pulses of sedimentary manganese deposition (Spinks et al., 2022; Robbins et al., 2023; Fig. 10A).

The Mn-shuttle driven mechanism explored here would have operated efficiently during the Paleoproterozoic (~2.3–2.05 Ga), establishing a link between primary kutnahorite formation and massive fabric-retentive dolomite precipitation (e.g.,Préat et al., 2011; Nzamba et al., 2026). This coupling persisted into the Mesoproterozoic, where dolomite abundance exhibits a relative peak. Notably, during the Calymmian-Ectasian (1.6–1.2 Ga), a sedimentary successions in the McArthur Basin host massive, fabric-retentive dolostones that preserve early eukaryotic cells and their Mn-mineralized sheaths (Muir, 1983). This specific association supports the hypothesis of Mn-catalysis as a critical microbial cell-fossilization agent in ancient carbonate platforms (Bontognali, 2019). Although the Mesoproterozoic was characterized by tectonic stability and expanding euxinia—conditions that possibly disrupted the long-range transport of hydrothermal Mn(II) required for massive ore formation (Poulton et al., 2010; Planavsky et al., 2014; Robbins et al., 2023)—newly quantified sedimentary Mn data challenge the concept of a complete mechanistic hiatus in shallow marine Mn-cycling, required for Mn-carbonate deposition (Spinks et al., 2022; Xu et al., 2025). Instead, the data suggest that the requisite redox-stratified water columns were maintained locally, preventing a total collapse of the Mn-shuttle dolomite coupling.

The dynamic re-emerged in the Neoproterozoic. High terrigenous Mn and silica fluxes and benthic microbial primary productivity during the Tonian (Liang et al., 2025) and Cryogenian–Ediacaran (Fang and Xu 2022; Cai et al., 2023) re-established conditions for syndiagenetic, fabric retentive dolomite formation (e.g., Liang et al., 2025; Hood et al., 2011; Stacey et al., 2023). Statistical analysis reveals positive correlation ($\rho = 0.50$) between dolomite abundance and manganese ores in the Precambrian (Supplementary Data 2). While statistical significance is inevitably constrained by the stochastic preservation of massive Mn ores and the inherent discontinuity of ancient dolostone abundance determinations (Petrash et al., 2017), this strong monotonic relationship supports that widespread redox stratification not

519 only favored Mn accumulation but simultaneously sustained the elusive seawater chemistry,
520 pervasive in the Proterozoic and recurrent in the Phanerozoic, that seems to be requisite for
521 the widespread deposition of syndiagenetic dolomicrite (Chang et al., 2020).

522 *4.3.2. Phanerozoic decoupling and restriction to continental basins*

523 The Phanerozoic record displays a contrasting negative correlation. ρ = -0.80,
524 marking a quantitative reversal in the relationship (Supplementary Data 2). This change
525 reflects the fundamental decoupling of these systems in oxygenated oceans and underscore
526 the shift in paragenesis of Mn deposits, as the drivers of massive manganese precipitation
527 (deep-ocean redox boundaries) became spatially and chemically separated from the loci of
528 shallow-marine dolomitization. In other words, as the Earth system transitioned toward a
529 fully oxygenated state (Fig. 10B), the ventilation of the deep ocean fundamentally disrupted
530 the shallow-water Mn-shuttle (Spinks et al., 2022; Chen et al., 2023; Robbins et al., 2023)
531 required for the ancient dolomite-forming engine proposed here.

532 As Mn-carbonates progressively gave way to Phanerozoic oxidized phases (Johnson
533 et al., 2016), dolomite formation became increasingly restricted. However, this long-term
534 decoupling was punctuated during intervals of Paleozoic and Mesozoic oceanic anoxia (Fig.
535 10B; Zhang et al., 2020; Li et al., 2021), when oceanographic conditions needed for shallow-
536 marine Mn-cycling were transiently re-established (Robbins et al., 2023). By the Neogene,
537 the Mn-templating mechanism for dolomite did not vanish but retreated, persisting in non-
538 marine settings such as rift lakes, where conditions analogue to the Mn-redox dynamics of
539 the Precambrian ocean existed (e.g., McCormack et al., 2024; Petrash et al., 2025).
540 Observations in post-Pliocene sabkha deposits (Chafetz et al., 1999; Bontognali et al., 2010;
541 Di Loreto et al., 2021) suggest that analogue (bio)geochemical conditions may also be locally
542 maintained in modern costal settings.

5. Conclusions and future work

We demonstrate that coupling manganese redox cycling with carboxyl functionalization unlocks a kinetically facile, non-classical pathway for the low-temperature formation of dolomite-group minerals. Our results show that electrochemical modulation accelerates Mn sequestration by over 60% compared to passive controls, stabilizing a metastable kutnahoritic precursor. This intermediate circumvents the high activation energy of Mg^{2+} dehydration, acting as a structural template that lowers the barrier for the heteroepitaxial nucleation of disordered dolomite in <24 h. The identification of mesocrystalline architectures, likely formed via crystallization by particle attachment, provides a physical explanation for the textural preservation of delicate features exceptionally observed in certain dolostones in the rock record. Unlike disruptive dissolution-reprecipitation models, this mechanism allows for compositional evolution while retaining primary aggregate morphology. Finally, our model offers a unifying explanation for the stratigraphic distribution of dolomite. We attribute the pervasive nature of Precambrian dolostones to the widespread availability of dissolved Mn(II) in redox-stratified ancient basins. Furthermore, we explain the distribution of massive dolomite in the Phanerozoic as a consequence of the spatial decoupling of manganese redox cycling from shallow carbonate platforms.

5.1. Future work

Moving forward, a significant technical hurdle remains the preparation of optimal FIB lamellae from these inherently friable, polycrystalline aggregates. While single-crystal diffraction would theoretically provide the definitive resolution for cation ordering, the pervasive polycrystalline nature of the spheroid precluded the isolation of discrete, defect-free domains large enough for standard tilt-series analysis. Consequently, future work must focus on optimizing ion polishing protocols—potentially identifying rare single-crystal domains—to achieve the ideal electron transparency ($(\lambda)^{-1} < 0.5$) required to resolve whether

faint superlattice reflections are present. Simultaneously, future research should prioritize constraining specific isotopic fractionation factors (e.g., $\delta^{26}Mg$, $\delta^{13}C$-$\delta^{18}O$, Δ_{47}-Δ_{48} REE systematics) associated with this pathway, and with extended synthesis until electrode passivation. To achieve this, experimental redesign can transition from closed-system batch reactors to continuous-flow chemostat setups under controlled pCO_2 atmospheres. Reengineering of the precipitation apparatus may allocate future work to systematically target the saturation states characteristic of ancient 'greenhouse' intervals. By clamping reactant activities (e.g., via external DIC buffering), it could be possible to effectively mitigate the cation depletion artifacts (Rayleigh fractionation) driven by rapid precursor precipitation. This steady-state approach would enable the precise determination of equilibrium distribution coefficients (K_D), which otherwise remain elusive in the compositionally drifting regimes typical of low-temperature dolomite synthesis.

Data availability

Data, including Python codes, are available through Zenodo at 10.5281/zenodo.18499776

Acknowledgement

This is a contribution to the Strategic Research Plan of The Czech Geological Survey (DKRVO/CGS 2023-2027, 311670). This study received funding from the EU Horizon Europe research and innovation programme under grant agreement No 101131765 (EXCITE2) for Transnational Access to Advanced Microscopy facilities at Utrecht University. We thank František Laufek (CGS) for conducting the XRD analysis of the residual solid phase, and Alireza Chogani for support during FIB-SEM preparation and (S)TEM analyses.

References

591 Aljinović, D., Richoz, S., Smirčić, D., Chen, Y., Nestell, G., Jazvac, I., Petrash, D.A., 2025.
592 Features and dolomitizing mechanisms in inner platform facies across the Permian–Triassic
593 boundary (External Dinarides, Croatia). *Sedimentology* 72, 822–843.

594 Bontognali, T.R.R., Vasconcelos, C., Warthmann, R.J., Bernasconi, S.M., Dupraz, C.,
595 Strohmenger, C.J., McKenzie, J.A., 2010. Dolomite formation within microbial mats in the
596 coastal sabkha of Abu Dhabi (United Arab Emirates). *Sedimentology* 57, 824–844.

597 Bontognali, T.R.R., 2019. Anoxygenic phototrophs and the forgotten art of making dolomite.
598 *Geology* 47, 591–592.

599 Böttcher, M.E., 1998. Manganese(II) partitioning during experimental precipitation of
600 rhodochrosite-calcite solid-solutions from aqueous solutions. *Mar. Chem.* 62, 287–297.

601 Böttcher, M.E., Dietzel, M., 2010. Metal-ion partitioning during low-temperature
602 precipitation and dissolution of anhydrous carbonates and sulfates. *EMU Notes Mineral.* 10,
603 139–187.

604 Cai, Y., Wallace, M.W., Hua, H., Hood, A., 2023. Interlinked marine cycles of methane,
605 manganese, and sulfate in the post-Marinoan Doushantuo cap dolostone. *Geochim.*
606 *Cosmochim. Acta* 346, 160–179.

607 Chafetz, H.S., Imerito-Tetzlaff, A.A., Zhang, J., 1999. Stable-isotope and elemental trends in
608 Pleistocene sabkha dolomites: Descending meteoric water vs. sulfate reduction. *J.*
609 *Sediment. Res.* 69, 256–266.

610 Chang, B., Li, C., Liu, D., Foster, I., Tripati, A., Lloyd, M.K., Immenhauser, A., 2020.
611 Massive formation of early diagenetic dolomite in the Ediacaran ocean: Constraints on the
612 “dolomite problem”. *Proc. Natl. Acad. Sci. U.S.A.* 117, 5522–5529.

613 Chen, G., Cheng, Q., Lyons, T.W., Shen, J., Agterberg, F., Huang, N., Zhao, M., 2022.
614 Reconstructing Earth's atmospheric oxygenation history using machine learning. *Nat.*
615 *Commun.* 13, 586.

616 Chen, F., Wang, Q., Pufahl, P.K., Matheson, E.J., Xian, H., Nan, J., Ma, H., Deng, J., 2023.
617 Carbonate-hosted manganese deposits and ocean anoxia. *Earth Planet. Sci. Lett.* 622,
618 118385.

619 Cölfen, H., Mann, S., 2003. Higher-order organization by mesoscale self-assembly and
620 transformation of hybrid nanostructures. *Angew. Chem. Int. Ed.* 42, 2350–2365.

621 De Yoreo, J.J., Gilbert, P.U.P.A., Sommerdijk, N.A.J.M., Penn, R.L., Whitelam, S., Joester,
622 D., Zhang, H., Rimer, J.D., Navrotsky, A., Banfield, J.F., Wallace, A.F., Michel, F.M.,
623 Meldrum, F.C., Cölfen, H., Dove, P., 2015. Crystallization by particle attachment in
624 synthetic, biogenic, and geologic environments. *Science* 349, 1–9.

625 Di Loreto, Z.A., Garg, S., Bontognali, T.R., Dittrich, M., 2021. Modern dolomite formation
626 caused by seasonal cycling of oxygenic phototrophs and anoxygenic phototrophs in a
627 hypersaline sabkha. *Sci. Rep.* 11, 4170.

628 Egerton, R.F., 2011. *Electron Energy-Loss Spectroscopy in the Electron Microscope*, 3rd ed.
629 Springer, New York.

630 Fang, Y., Xu, H., 2022. Coupled dolomite and silica precipitation from continental
631 weathering during deglaciation of the Marinoan Snowball Earth. *Precambrian Res.* 380,
632 106824.

633 Goldsmith, J.R., Graf, D.L., 1960. Subsolidus relations in the system CaCO3-MgCO3-
634 MnCO3. *J. Geol.* 68, 324–335.

635 Graf, D.L., Goldsmith, J.R., 1956. Some hydrothermal syntheses of dolomite and
636 protodolomite. *J. Geol.* 64, 173–186.

637 Gránásy, L., Pusztai, T., Tegze, G., Warren, J.A., Douglas, J.F., 2005. Growth and form of
638 spherulites. *Phys. Rev. E* 72, 011605.

639 Han, Z., Zhang, F., Farfan, G.A., Xu, H., 2024. Dissolved Mn2+ promotes microbially-
640 catalyzed protodolomite precipitation in brackish oxidized water. *Chem. Geol.* 650, 121986.

641 Helm, L., Merbach, A.E., 2005. Inorganic and bioinorganic solvent exchange mechanisms.
642 *Chem. Rev.* 105, 1923–1959.

643 Higgins, S.R., Hu, X., 2005. Self-limiting growth on dolomite (104) surfaces. *Geochim.*
644 *Cosmochim. Acta* 69, 2085–2094.

645 Hood, A.v.S., Wallace, M.W., Drysdale, R.N., 2011. Neoproterozoic marine dolomite
646 hardgrounds and their relationship to cap dolomites. *Precambrian Res.* 188, 118–134.

647 Jakob, K.S., Walsh, A., Reuter, K., Margraf, J.T., 2025. Learning crystallographic disorder:
648 Bridging prediction and experiment in materials discovery. *Adv. Mater.*, e14226.

649 Ji, Z., Hu, M., Xin, H.L., 2023. Mn-EdgeNet for accurate decomposition of mixed oxidation
650 states for Mn XAS and EELS L2,3 edges without reference and calibration. *Sci. Rep.* 13,
651 14132.

652 Ji, D., Park, J.M., Oh, M.S., Nguyen, T.L., Shin, H., Kim, S.L., Kim, D., Kim, J., 2022.
653 Superstrong, superstiff, and conductive alginate hydrogels. *Nat. Commun.* 13, 3019.

654 Johnson, J.E., Webb, S.M., Ma, C., Fischer, W.W., 2016. Manganese mineralogy and
655 diagenesis in the sedimentary rock record. *Geochim. Cosmochim. Acta* 173, 210–231.

656 Jørgensen, B.B., Revsbech, N.P., Blackburn, T.H., Cohen, Y., 1979. Diurnal cycle of oxygen
657 and sulfide microgradients and microbial photosynthesis in a cyanobacterial mat sediment.
658 *Appl. Environ. Microbiol.* 38, 46–58.

659 Katsikopoulos, D., Fernández-González, Á., Prieto, M., 2009. Crystallization behaviour of
660 the (Mn,Ca)CO3 solid solution in silica gel: nucleation, growth and zoning phenomena.
661 *Mineral. Mag.* 73, 269–284.

662 Li, M., Wignall, P.B., Dai, X., Hu, M., Song, H., 2021. Phanerozoic variation in dolomite
663 abundance linked to oceanic anoxia. *Geology* 49, 698–702.

664 Luther, G.W., 2005. Thermodynamics and kinetics of manganese (II) oxidation and Mn (IV)
665 reduction in the environment: Two one-electron transfer steps versus a single two-electron
666 step. *Geomicrobiol. J.* 22, 195–203.

667 Marcus, Y., 1987. Thermodynamics of ion hydration and its interpretation in terms of a
668 common model. *Pure Appl. Chem.* 59, 1093–1101.

669 McCormack, J., Bontognali, T.R.R., Immenhauser, A., Kwiecien, O., 2018. Controls on
670 cyclic formation of Quaternary early diagenetic dolomite. *Geophys. Res. Lett.* 45, 3625–
671 3634.

672 McKenzie, J.A., 1991. The dolomite problem; an outstanding controversy. In: *Controversies*
673 *in Modern Geology: Evolution of Geological Theories in Sedimentology, Earth History and*
674 *Tectonics*. Academic Press, pp. 37–54.

675 Meister, P.H., Frisia, S., Dódony, I., Pekker, P., Molnár, Z., Neuhuber, S., Gier, S., Kovács,
676 I., Demény, A., Pósfai, M., 2023. Nanoscale pathway of modern dolomite formation in a
677 shallow, alkaline lake. *Cryst. Growth Des.* 23, 3202–3212.

678 Meng, R., Han, Z., Gao, X., Zhao, Y., Han, C., Han, Y., Yang, R., Li, S., Liu, F., Tucker,
679 M.E., Yan, H., 2024. Dissolved ammonia catalyzes proto-dolomite precipitation at Earth
680 surface temperature. *Earth Planet. Sci. Lett.* 646, 119012.

681 Mercedes-Martín, R., Rogerson, M.R., Brasier, A.T., Vonhof, H.B., Prior, T.J., Fellows,
682 S.M., Pedley, H.M., 2016. Growing spherulitic calcite grains in saline, hyperalkaline lakes:

683 experimental evaluation of the effects of Mg-clays and organic acids. *Sediment. Geol.* 335,
684 93–102.

685 Mucci, A., 1988. Manganese uptake during calcite precipitation from seawater: Conditions
686 leading to the formation of a pseudo-kutnahorite. *Geochim. Cosmochim. Acta* 52, 1859–
687 1868.

688 Mucci, A., 2004. The behavior of mixed Ca–Mn carbonates in water and seawater: Controls
689 of manganese concentrations in marine porewaters. *Aquat. Geochem.* 10, 139–169.

690 Muir, M.D., 1983. Proterozoic microfossils from the Mara Dolomite Member, Emmerugga
691 Dolomite, McArthur Group, from the Northern Territory, Australia. *Bot. J. Linn. Soc.* 86,
692 1–18.

693 Nielsen, L.P., Risgaard-Petersen, N., Fossing, H., Christensen, P.B., Sayama, M., 2010.
694 Electric currents couple spatially separated biogeochemical processes in marine sediment.
695 *Nature* 463, 1071–1074.

696 Nzamba, K.X., Juhkama, H.R., Moussavou, M., Mayika, K.B., Kreitsmann, T., Lepland, A.,
697 Prave, A.R., Kirsimäe, K., 2026. Carbonate diagenesis and Mn-carbonate formation in the
698 Paleoproterozoic Francevillian succession (Lastoursville sub-basin) of Gabon. *J. Afr. Earth*
699 *Sci.* 235, 105971.

700 Peacor, D.R., Essene, E.J., Gaines, A.M., 1987. Petrologic and crystal-chemical implications
701 of cation order-disorder in kutnahorite [CaMn(CO3)2]. *Am. Mineral.* 72, 319–328.

702 Petrash, D.A., Roeser, P., Kříbek, B., Staudigel, P.T., Bernecker, M., Jačková, I., Čejková,
703 B., Kochergina, Y.V.E., Koubová, M., Křížová, Š., Knésl, I., Laufek, F., Böttcher, M.E.,
704 Della Porta, G., Fiebig, J., 2025. Drivers of episodic carbonate cementation during the
705 Miocene Climatic Optimum in a paleolake of the Eger Rift (Czech Republic). *Geochim.*
706 *Cosmochim. Acta* 407, 47–66.

Petrash, D.A., Bialik, O.M., Staudigel, P.T., Konhauser, K.O., Budd, D.A., 2021. Biogeochemical reappraisal of the freshwater–seawater mixing-zone diagenetic model. *Sedimentology* 68, 1797–1830.

Petrash, D.A., Lalonde, S.V., González-Guayaquil, A., Konhauser, K.O., Méndez-Vicente, A., 2015. Can Mn–S redox cycling drive sedimentary dolomite formation? A hypothesis. *Geology*.

Petrash, D.A., Bialik, O.M., Bontognali, T.R., Vasconcelos, C., Roberts, J.A., McKenzie, J.A., Konhauser, K.O., 2017. Microbially catalyzed dolomite formation: From near-surface to burial. *Earth-Sci. Rev.* 171, 558–582.

Petrash, D.A., Lalonde, S.V., Raudsepp, M., Konhauser, K.O., 2011. Assessing the importance of organic matrix materials in biofilm chemical reactivity: Insights from proton and cadmium adsorption onto the commercially available biopolymer alginate. *Geomicrobiol. J.* 28, 266–273.

Pina, C.M., Pimentel, C., Crespo, A., 2022. The dolomite problem: A matter of time. *ACS Earth Space Chem.* 6, 1468–1471.

Planavsky, N.J., Reinhard, C.T., Wang, X., Thomson, D., McGoldrick, P., Rainbird, R.H., Johnson, T., Fischer, W.W., Lyons, T.W., 2014. Low mid-Proterozoic atmospheric oxygen levels and the delayed rise of animals. *Science* 346, 635–638.

Poulton, S.W., Fralick, P.W., Canfield, D.E., 2010. Spatial variability in oceanic redox structure 1.8 billion years ago. *Nat. Geosci.* 3, 486–490.

Préat, A., Bouton, P., Thiéblemont, D., Prian, J.P., Ndounze, S.S., Delpomdor, F., 2011. Paleoproterozoic high δ13C dolomites from the Lastoursville and Franceville basins (SE Gabon): Stratigraphic and synsedimentary subsidence implications. *Precambrian Res.* 189, 212–228.

731 Purgstaller, B., Mavromatis, V., Immenhauser, A., Dietzel, M., 2016. Transformation of Mg-
732 bearing amorphous calcium carbonate to Mg-calcite—In situ monitoring. *Geochim.*
733 *Cosmochim. Acta* 174, 180–195.

734 Purgstaller, B., Goetschl, K.E., Mavromatis, V., 2019. Solubility investigations in the
735 amorphous calcium magnesium carbonate system. *CrystEngComm* 21, 155–164.

736 Robbins, L.J., Fakhraee, M., Smith, A.J.B., Bishop, B.A., Swanner, E.D., Peacock, C.L.,
737 Wang, C.L., Planavsky, N.J., Reinhard, C.T., Crowe, S.A., Lyons, T.W., 2023. Manganese
738 oxides, Earth surface oxygenation, and the rise of oxygenic photosynthesis. *Earth-Sci. Rev.*
739 239, 104368.

740 Rosenberg, P.E., Foit Jr., F.F., 1979. The stability of dolomite in aqueous solution: An
741 experimental investigation at 25° to 275°C. *Geochim. Cosmochim. Acta* 43, 951–955.

742 Shang, H., 2023. Dichotomous effects of oxidative metabolisms: A theoretical perspective on
743 the dolomite problem. *Glob. Planet. Change* 222, 104041.

744 Spinks, S.C., Sperling, E.A., Thorne, R.L., LaFountain, F., White, A.J.R., Armstrong, J.,
745 Woltering, M., Tyler, I.M., 2023. Mesoproterozoic surface oxygenation accompanied major
746 sedimentary manganese deposition at 1.4 and 1.1 Ga. *Geobiology* 21, 28–43.

747 Stacey, J., Hood, A.v.S., Wallace, M.W., 2023. Persistent late Tonian shallow marine anoxia
748 and euxinia. *Precambrian Res.* 397, 107207.

749 Sunagawa, I., 2005. *Crystals: Growth, Morphology, and Perfection*. Cambridge University
750 Press, Cambridge.

751 Tordi, P., Ridi, F., Samorì, P., Bonini, M., 2025. Cation-alginate complexes and their
752 hydrogels: A powerful toolkit for the development of next-generation sustainable functional
753 materials. *Adv. Funct. Mater.* 35, 2416390.

754 Vandeginste, V., Snell, O., Hall, M.R., Steer, E., Vandeginste, A., 2019. Acceleration of
755 dolomitization by zinc in saline waters. *Nat. Commun.* 10, 1851.

756 Van Tendeloo, G., Amelinckx, S., De Fontaine, D., 1985. On the nature of the 'short-range
757 order' in 1/2{hkl} alloys. *Acta Crystallogr. B* 41, 281–292.

758 Wang, D., Wallace, A.F., De Yoreo, J.J., Dove, P.M., 2009. Carboxylated molecules regulate
759 magnesium content of amorphous calcium carbonates during calcification. *Proc. Natl.*
760 *Acad. Sci. U.S.A.* 106, 21511–21516.

761 Xu, L., Yu, W., Konhauser, K.O., Guo, H., Jin, S., Ma, P., Du, Y., 2025. Genesis of
762 manganese-rich deposits in the Mesoproterozoic Gaoyuzhuang Formation, North China:
763 Implications for atmospheric redox state and early eukaryote evolution. *Palaeogeogr.*
764 *Palaeoclimatol. Palaeoecol.* 668, 112924.

765 Zhang, F., Xu, H., Konishi, H., Roden, E.E., 2012a. Polysaccharide catalyzed nucleation and
766 growth of disordered dolomite: A potential precursor of sedimentary dolomite. *Am.*
767 *Mineral.* 98, 2070–2076.

768 Zhang, F., Xu, H., Konishi, H., Roden, E.E., 2012b. Dissolved sulfide-catalyzed precipitation
769 of disordered dolomite: Implications for the formation mechanism of sedimentary dolomite.
770 *Geochim. Cosmochim. Acta* 97, 148–165.

771 Zhang, F., Shen, S.Z., Cui, Y., Lenton, T.M., Dahl, T.W., Zhang, H., Zheng, Q.F., Wang, W.,
772 Krainer, K., Anbar, A.D., 2020. Two distinct episodes of marine anoxia during the
773 Permian-Triassic crisis evidenced by uranium isotopes in marine dolostones. *Geochim.*
774 *Cosmochim. Acta* 287, 165–179.

775

776

777 **FIGURES**

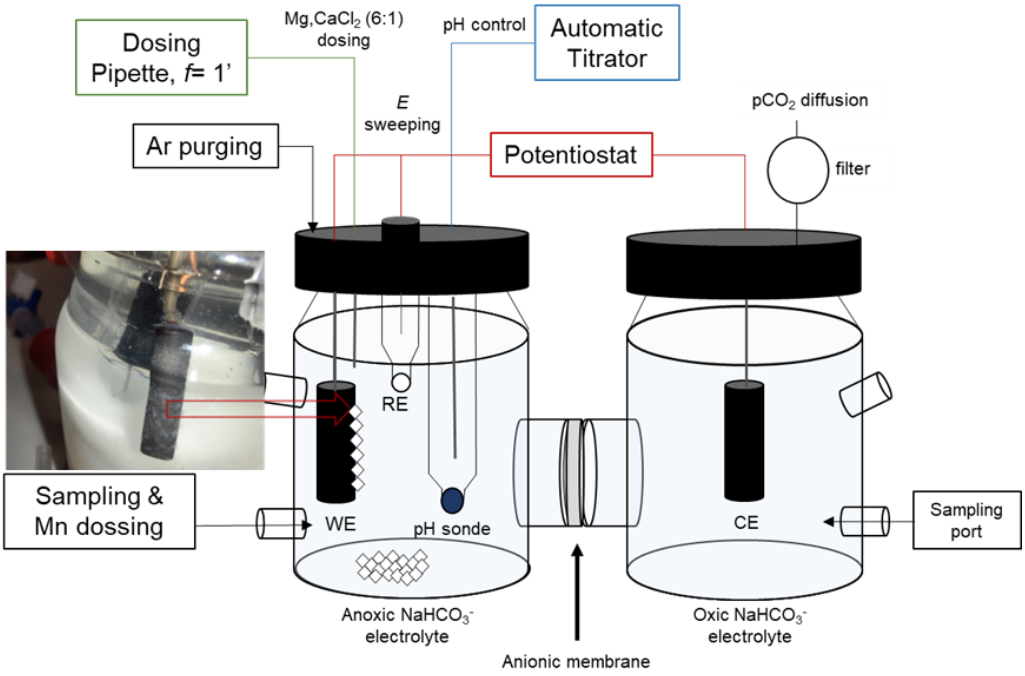

778

779 **Figure 1. Schematic of the two-cell electrochemical precipitation apparatus**. Two
780 150 mL borosilicate glass reaction vessels were connected via an anodic membrane. System
781 hydrochemistry was controlled using an automatic pH-stat titrator and a potentiostat applying
782 continuous potential sweeps. One cell, containing the working electrode (WE) and reference
783 electrode (RE), was maintained under an Ar atmosphere, while the other, housing the counter
784 electrode (CE), remained in equilibrium with air. Both WE and CE had surface areas of 4.2
785 $cm^{2.}$ The electrolyte consisted of $NaHCO_3$ solution. Following pre-titration (see test for
786 details), the cation feedstock was introduced at 1' intervals using a dosing pipette (n=20); a
787 single $MnCl_2$ dose was at t ~ 5' . The inset shows WE and surface precipitates, with residual
788 precipitates formed quasi-instantaneously in solution upon reactant additions. Attention of
789 this study is placed on the surface precipitates.

790

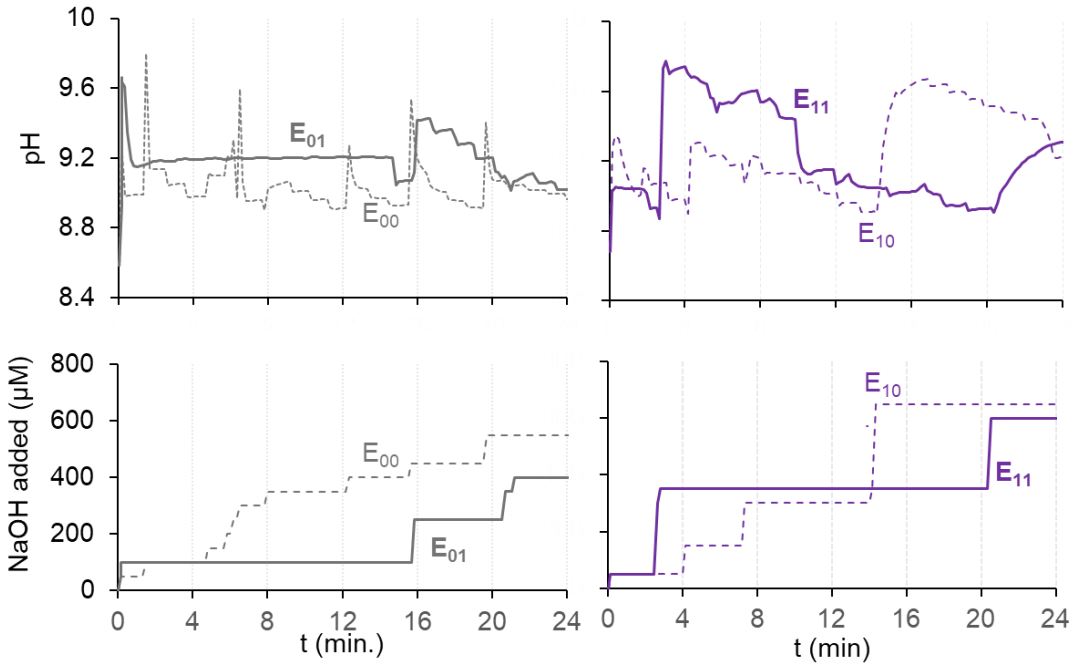

791

792 **Figure 2**. Experimental pH and NaOH additions during carbonate synthesis under four
793 conditions: control (E_{00}), electrochemistry only (E_{01}), functionalized only (E_{10}), and
794 combined (E_{11}). Electrochemistry and functionalization reduced titrant demand, enhancing
795 buffering.

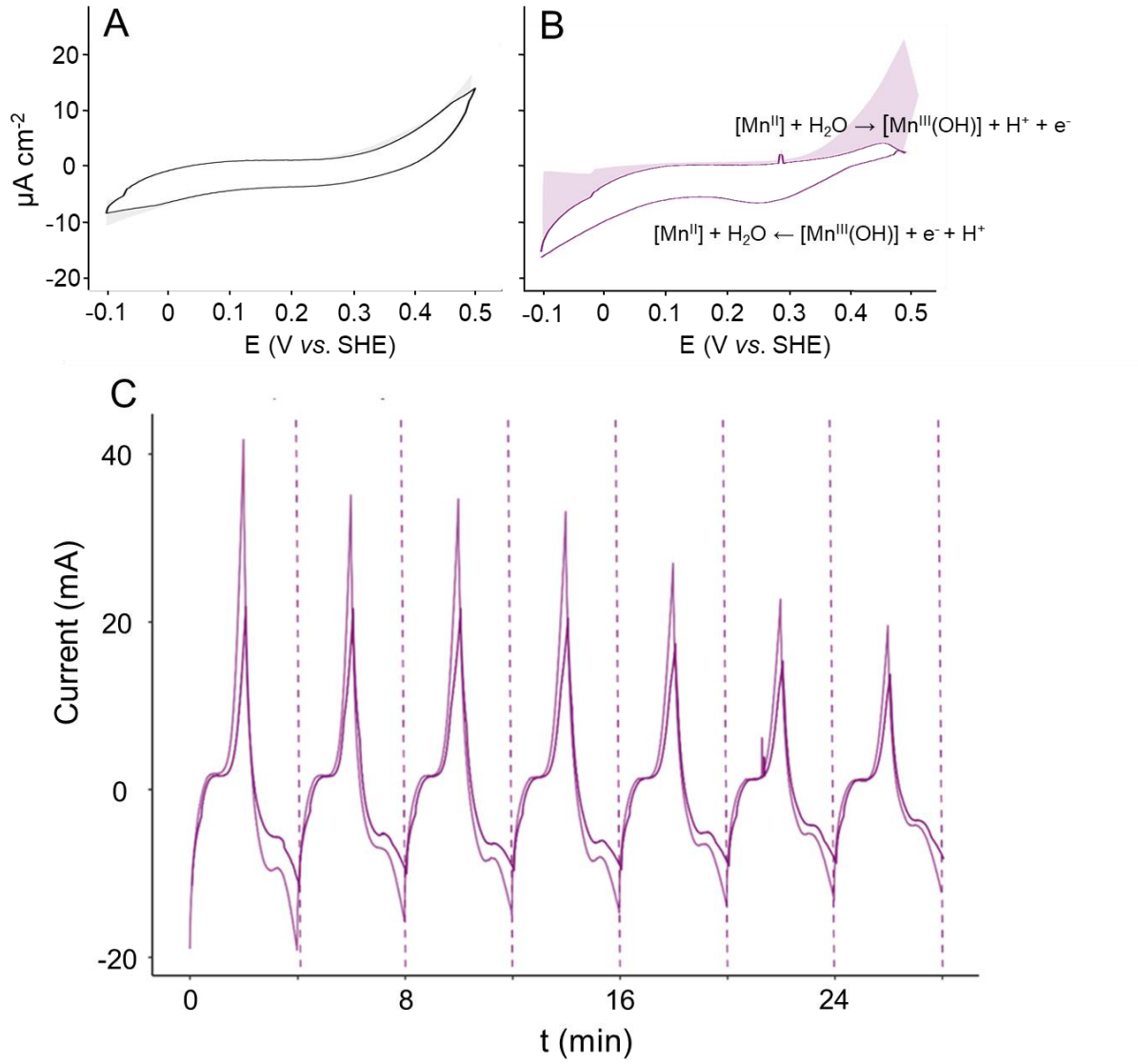

Figure 3. Electrochemical characterization of the Mn-functionalized system. Cyclic voltammograms (CV) recorded in carbonate-buffered electrolyte (E: [-0.1 to +0.5] V vs. SHE). (A) Control without functionalization exhibits a featureless profile characteristic of non-faradaic capacitive charging. (B) Carboxyl-functionalized hydrogel displays distinct quasi-reversible peaks, confirming active Mn redox cycling. Annotated equations detail the proposed proton-coupled electron transfer (PCET) mechanism: anodic oxidation coupled to hydrolysis (proton release) and cathodic reduction coupled to proton consumption. Solid lines denote average current density (j); shaded areas indicate standard deviation. (C) Temporal evolution of the current response (I) over 28 minutes in the functionalized system (E_{11}). Sharp peaks align with the 4-minute potential sweep periodicity (dashed lines). The progressive attenuation of peak intensity indicates gradual electrode passivation, consistent with the formation of non-conductive carbonate precipitate.

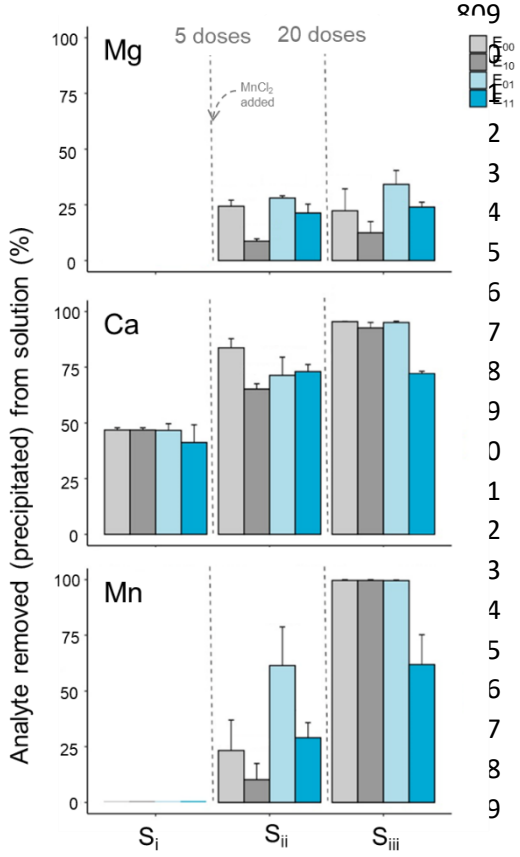

Figure 4. Percentage of Mg, Ca, and Mn removed (precipitated) from solution under four experimental conditions: without carboxyl groups (light grey), with carboxyl groups (dark grey), and their respective counterparts with electrochemical potential sweeping (light and dark blue). Samples were collected at three time points. These are S_i: 5' after start, with 5 doses of 1 mL $(Ca,Mg)Cl_2$ solution added to the system, and before the 10 mM $MnCl_2$ addition; S_{ii}: after 20', i.e., 20 doses of 1 mL of $(Ca,Mg)Cl_2$ solution; and S_{iii}: after the 24 h stabilization time lag. Consumption was calculated as the percentage difference between measured concentrations and maximum expected concentrations, i.e. @5' $\{[Mg]_{max}$= 21 mM, $[Ca]_{max}$= 3.6 mM, $[Mn]_{max}$= 0.0 mM$\}$; @20' and 24 h:$\{[Mg]_{max}$= 86 mM, $[Ca]_{max}$= 14 mM, $[Mn]_{max}$= 10 mM$\}$. Bars represent mean duplicate values, and whiskers indicate standard deviation based on duplicate experiments.

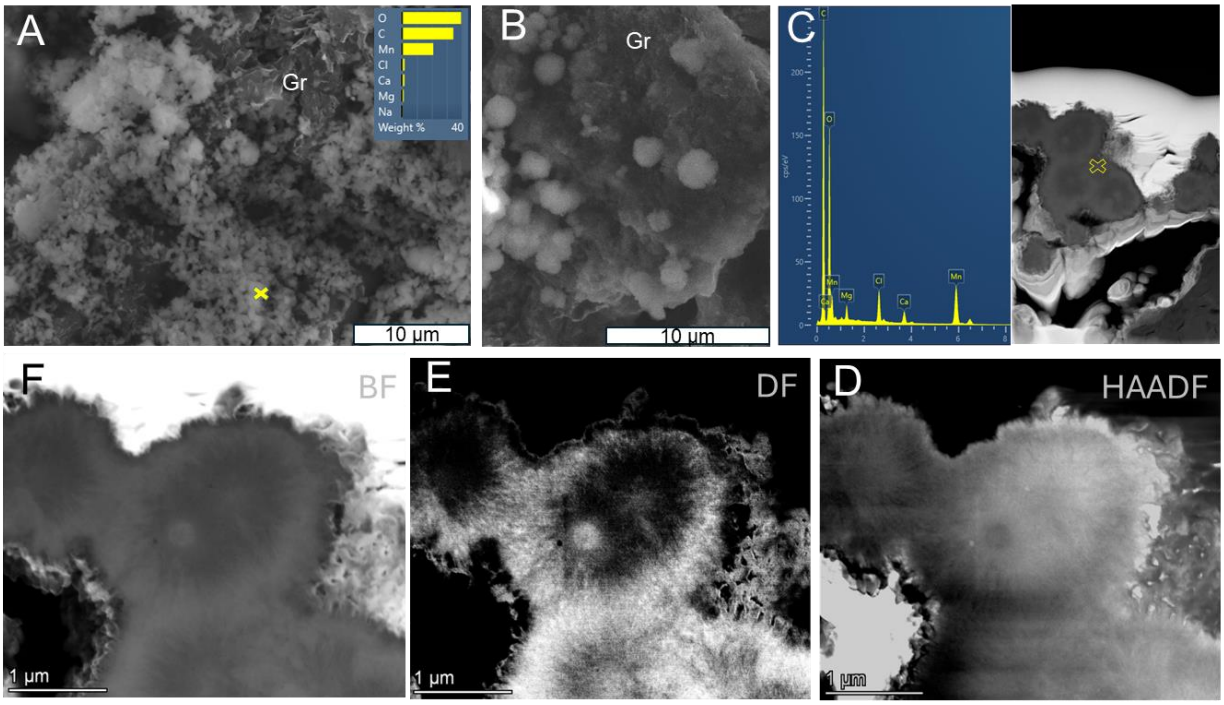

Figure 5. Solid phase characterization of carbonate precipitates in Control (E_{00}) vs. Functionalized (E_{10}) conditions. (A) SEM-EDS characterization of the control sample (E_{00}), where the absence of functionalization and cycling resulted in sparse, Mn-dominated precipitates (Mn >> Ca + Mg) with minimal surface accumulation. (B) SEM image of sample E_{10} (functionalization without electrochemical cycling), showing increased precipitate density and the formation of coherent carbonate spheroids on the graphite (Gr) substrate. (C) EDS spectrum of an E_{10} spheroid, confirming the phase as a manganous Mg-Ca carbonate. (D–F) Cross-sectional TEM analysis (HAADF, Dark Field, and Bright Field) of the E_{10} spheroids, revealing a spherulitic internal fabric composed of crystallites radiating outward from central nucleation centers.

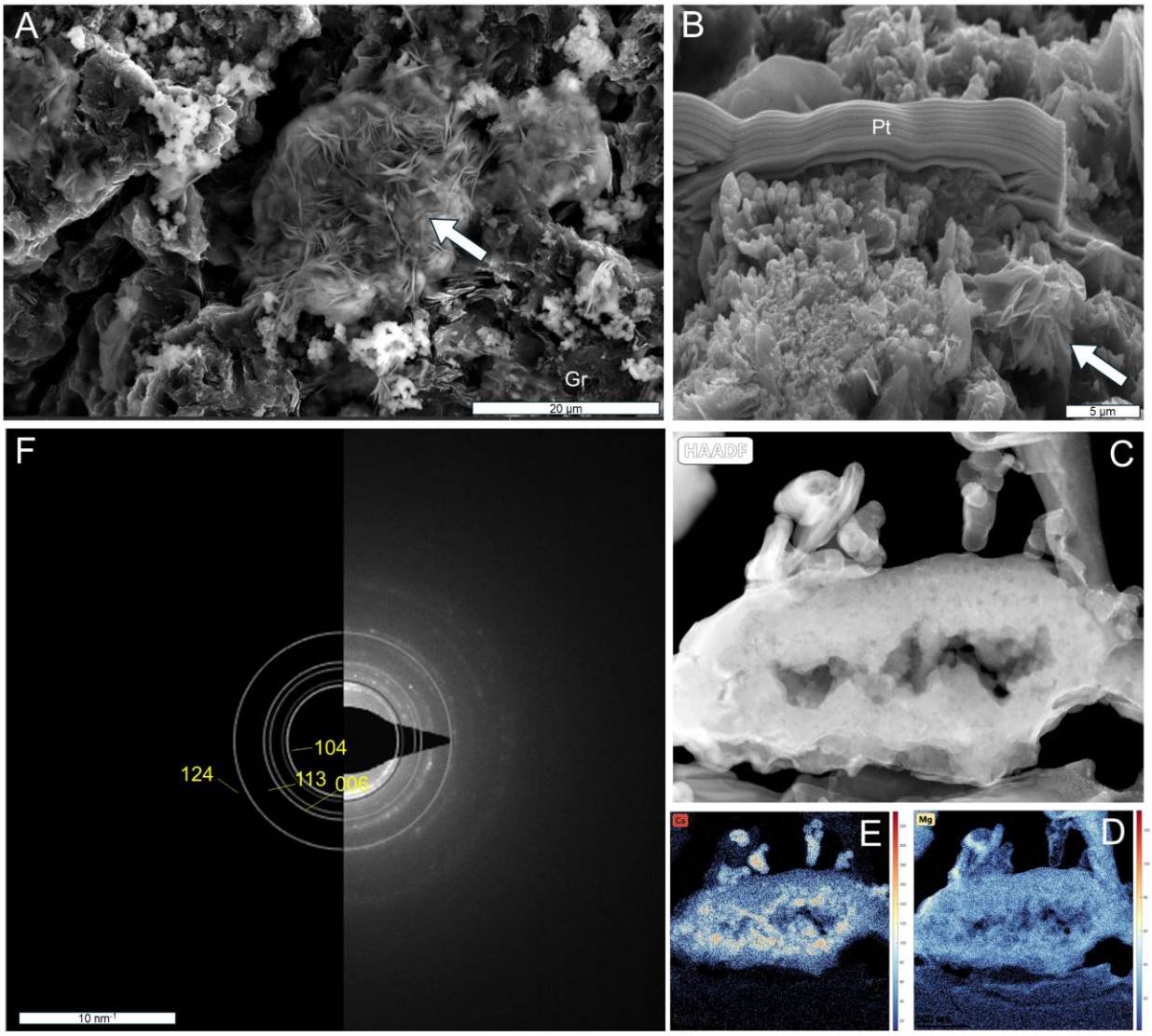

Figure 6. Morphology and structure of precipitates formed under electrochemical cycling without functionalization (E_{01}). (A) SEM of the electrode surface showing prominent rosette-like structures (arrow) intermixed with disperse, granular polycrystalline aggregates (B) FIB-milling site; the delicate rosettes (arrow) were unstable under the ion beam, leaving only the granular aggregates for analysis (C) STEM-HAADF cross-section revealing a porous, "vuggy" texture formed by coalesced nanocrystalline domains. Contrast variations highlight chemical zonation (inset mean EDS spectrum). (D–E) EDS maps contrasting the internal zonation of Ca with the homogeneously distributed Mg. (F) SAED pattern showing diffraction rings consistent with cation-substituted rhodochrosite lattice spacings.

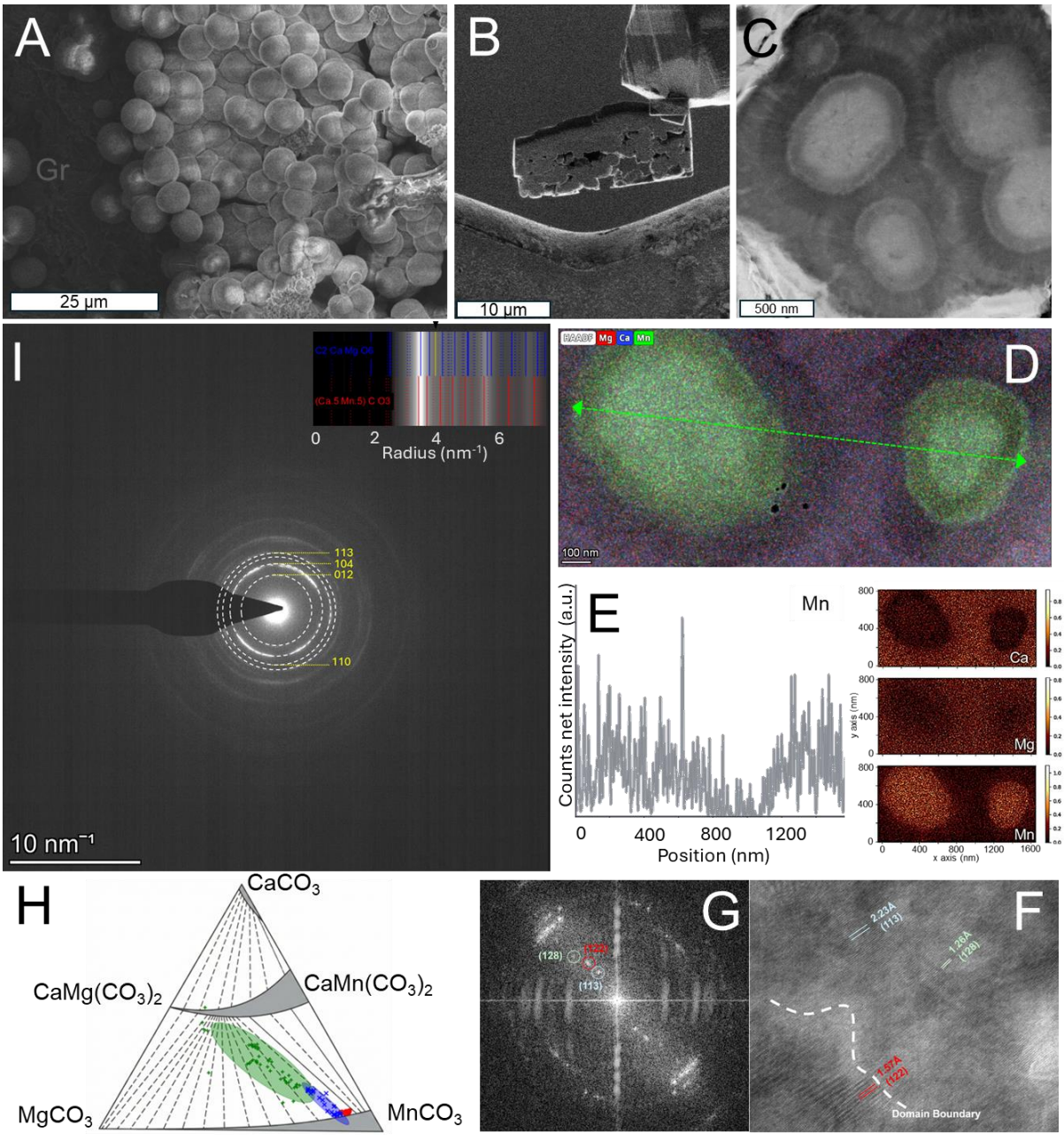

Figure 7. Multiscale characterization of Mn-templated protodolomite formed under electrochemical and carboxyl modulation (E_{11}). **(A–C) Morphology and texture: (A)** SEM micrograph showing the dense accumulation of spheroidal aggregates on the graphite electrode (Gr). **(B)** SEM view of a FIB-milled cross-section (lamella) extracted from the aggregate cluster. **(C)** STEM-HAADF image of the lamella, revealing the characteristic "eye-like" core-shell zonation and diverging sheaf texture. **(D–I) Nanostructure and chemistry**: **(D)** STEM-EDS composite map confirming cation partitioning: Mn-enriched cores (green) surrounded by Mg/Ca-rich cortices (red/blue). **(E)** EDS line-scan intensity profile (1.6 µm) for Mn across the aggregate (transect in D), showing the preferential sequestration of Mn in the core regions; the segregated distributions of Ca, Mg, and Fe are also shown. **(F)** High-resolution TEM (HRTEM) micrograph of a crystalline domain. The lattice fringes and the diffuse domain boundary (white dashed line) highlight the mosaic nanostructure, showing nanodomains (<30 nm) intergrowth together with different crystallographic orientations. **(G)**

Fast Fourier-Transform (FFT) of the HRTEM image **(H)** Compositional TEM-EDS data projected onto the $CaCO_3$-$MgCO_3$-$MnCO_3$ ternary plot, the low temperature two-phase manganoan carbonate stability fields/miscibility gap are shown (after Peacor et al.,1987). EDS data renormalized to [Ca] + [Mg] + [Fe] = 1. The confidence ellipses are calculated from the variance (scatter) of the data points. **(I)** SAED pattern acquired from the cortex with identified diffraction rings. The inset/overlay displays the theoretical ring positions for dolomite and kutnohorite, highlighting the expected location of the d_{015} superstructure reflection. This reflection may be highly attenuated by broadening and superposition of d_{104} peaks in polycrystalline matrices comprised of both minerals (see text for details).

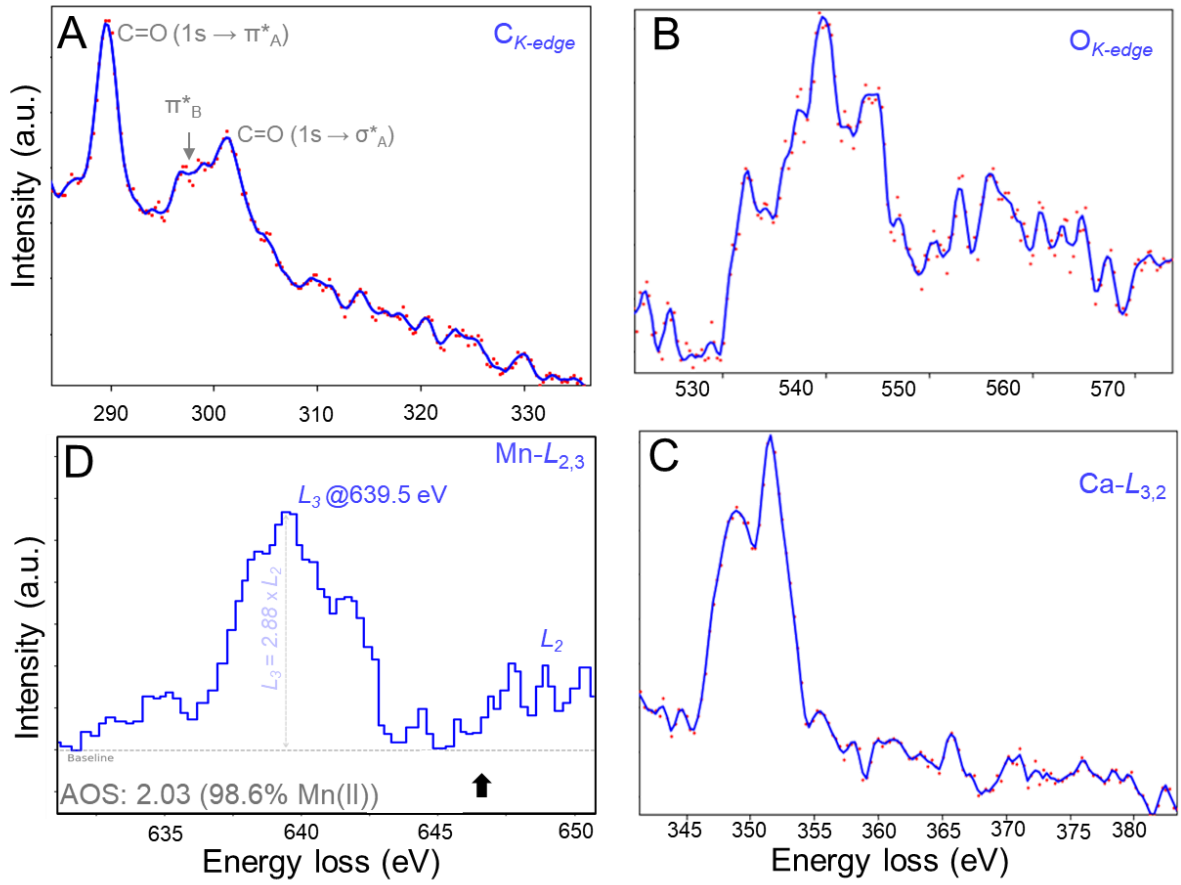

877

878 **Figure 8.** Representative core-loss EELS spectra acquired from the inner cortex region. (A)
879 Carbon K-edge showing the characteristic π∗ and σ∗ transitions of the carbonate. (B) Oxygen
880 K-edge exhibiting fine structure consistent with carbonate bonding. (C) Calcium $L_{3,2}$ -edge
881 displaying sharp white lines indicative of a crystalline coordination environment. (D)
882 Manganese $L_{2,3}$ edge spectrum. The data is presented as a raw step plot to preserve peak
883 shape fidelity. The analysis reveals a sharp L_3 maximum at 639.5 eV and an intensity ratio of
884 $L_3/L_2 \approx 2.88$, consistent with high-spin Mn(II). A key feature is the complete return to
885 baseline intensity in the inter-peak valley (~645 eV, black arrow), effectively ruling out
886 significant mixed-valence contributions.

887

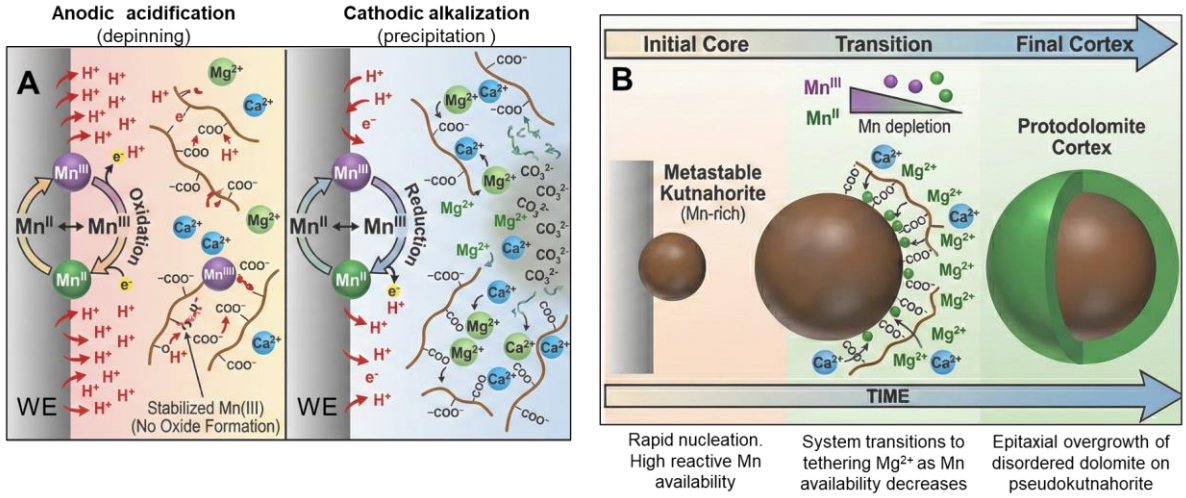

Fig. 9. Proposed mechanism of electrochemically induced dolomite growth. (A) The proton-coupled redox engine. At the working-electrode interface, anodic oxidation of Mn and concurrent water splitting generate Mn and protons (H^+). This drives anodic acidification, in the vicinity of the electrode which transiently protonates alginate ligands and causes the depinning of bound cations (Mg^{2+}, Ca^{2+}). The subsequent cathodic alkalization consumes protons, reactivating the ligands to bind cations and producing a local supersaturation spike. The carboxyl ligands form stabilized Mn complexes, acting as a kinetic brake that prevents oxide formation and sustains the quasi-reversible cycle. (B) Core-to-cortex evolution. Initially high concentrations of reactive Mn drive the rapid nucleation of a pseudo-kutnahorite template. As aqueous Mn availability progressively decreases (see transition wedge), the pumping mechanism shifts toward tethering the increasingly abundant Mg ions. These are delivered to the growth front, facilitating the epitaxial overgrowth of a protodolomite cortex.

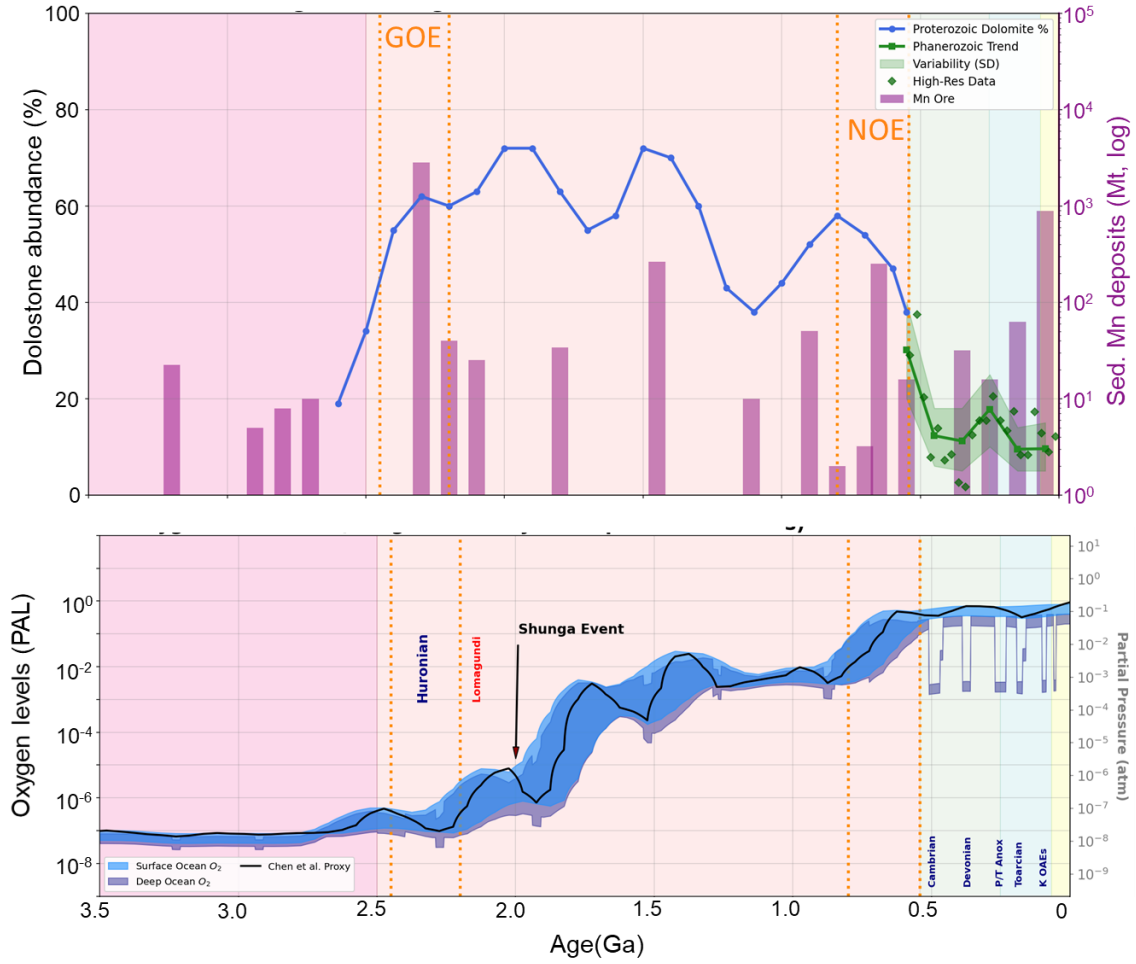

Figure. 10 Integrated evolution of global ocean redox conditions, carbonate mineralogy, and manganese deposition. (A) Secular trends in dolomite abundance (blue: Proterozoic; green: Phanerozoic mean ± SD; derived from Shang et al., 2023; Li et al., 2021) plotted against Mn ore deposits (purple bars; Robbins et al., 2023). Note the strong co-occurrence of dolomite peaks with Mn pulses in the Precambrian. (B) Evolution of oxygenation states (pO_2). Surface envelopes are calibrated to Chen et al. (2022). The deep ocean tracks surface conditions in the Mesoproterozoic but decouples during high-amplitude redox fluctuations: (i) the Great Oxidation Event (GOE) and Huronian glaciations; (ii) the Lomagundi-Jatuli overshoot; (iii) the Shunga Event oxygen crash; and (iv) the Neoproterozoic Oxygenation Event (NOE). In the Phanerozoic, the deep-water "Mn-pump" is largely suppressed, re-emerging only during transient Ocean Anoxic Events (e.g., P-Tr, Toarcian, K-OAEs) where deep waters dropped to <1% surface saturation.

TABLE

Table S1. Summary of aqueous geochemical evolution and cation removal efficiencies.

Parameter	Initial Phase (Doses 1–5)	End of titration (20 doses)[†] [‡]	Stabilization 24h[†]	Primary controlling factors
NaOH Titrant	**Delayed onset:** Lag in consumption (0–15 min) due to proton consumption from Mn(III) reduction	**Linear increase:** Steady demand to buffer proton release from precipitation	**Converged:** Total volume ~ 0.50–0.60 mL (0.25–0.30 mmol-eq OH^-) across all experiments.	Proton consumption by electrochemical Mn-reduction vs. alkalinity demand from carbonate equilibrium (HCO_3^- → $CO_3^{2-} + H^+$)
Mg removal	**Negligible:** No significant uptake observed.	**Variable:** 8.7 ± 1.1 % (E_{10}) to 28.0 ± 1.0% (E_{01}). Highest in electrochemical setups, but reduced by carboxyl (E_{11} < E_{01})	**Incomplete:** Slight increase (3-6%). Majority (66-87%) persists in solution.	Electrochemical treatment enhances Mg co-precipitation, but carboxyl functionalization partially mitigates this effect
Ca removal	**Rapid:** >40% removal prior to Mn addition (ACC formation)	**High:** 65.2 ± 2.4% to 83.7 ± 4.1% removal	**Near complete:** >95% removal, except E_{11} (~75%)	Initial homogeneous nucleation of ACC ; partially inhibited by ligand stabilization in E_{11}.
Mn removal	**N/A:** Mn added after Dose 5.	**Kinetic Response:** $E_{01} \gg E_{00}$, w./ E_{01} (61.4%) > E_{11} (29.0%) > E_{00} (23.3%) > E_{10} (10.2%)	**Complete vs. stabilized:** >99% removal in most units. Exception: E_{11} retains 25-38% in solution	Applied potential drives rapid sequestration; alginate in E_{11} stabilizes Mn(III) intermediates against precipitation

[†] Conditions denote E_{00} (control), E_{01} (electrochemistry only), E_{10} (functionalized only), and E_{11} (combined).
[‡] Removal (%)calculated relative to the total molar mass added to the H-cell reactor.

SUPPLEMENTARY MATERIAL

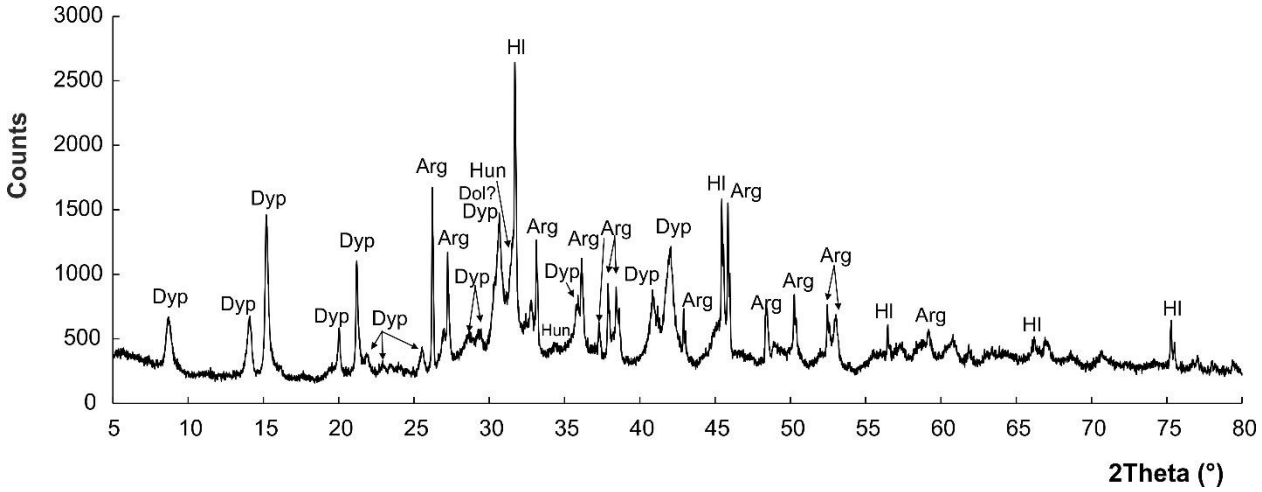

Fig. S1. 1-D X-ray diffraction pattern of the residual solid phase. The mineral assemblage was analyzed after complete evaporation of the parental H-cell solution at 25 °C. Identified phases include aragonite (Arg), dypingite, $Mg_5(CO3)_4(OH)_2 \cdot 5H_2O$ (Dyp), and halite. (Dyp) and halite.

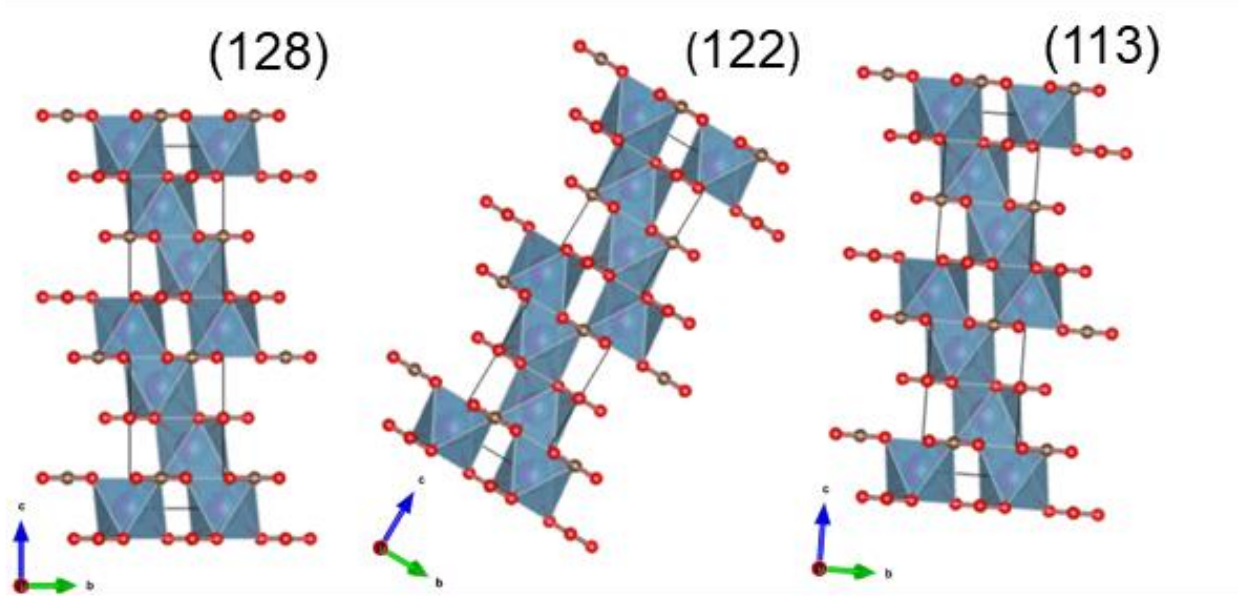

Figure S2 | Fast Fourier Transform (FFT) generated from the HRTEM micrograph in Figure 7F. The pattern displays discrete diffraction spots corresponding to the (128), (122), and (113) lattice planes. The characteristic arcing of these spots highlights the rotational mismatch between adjacent nanodomains, quantifying the crystallographic misorientations (~3 to 11º) associated with the mosaic fabric.

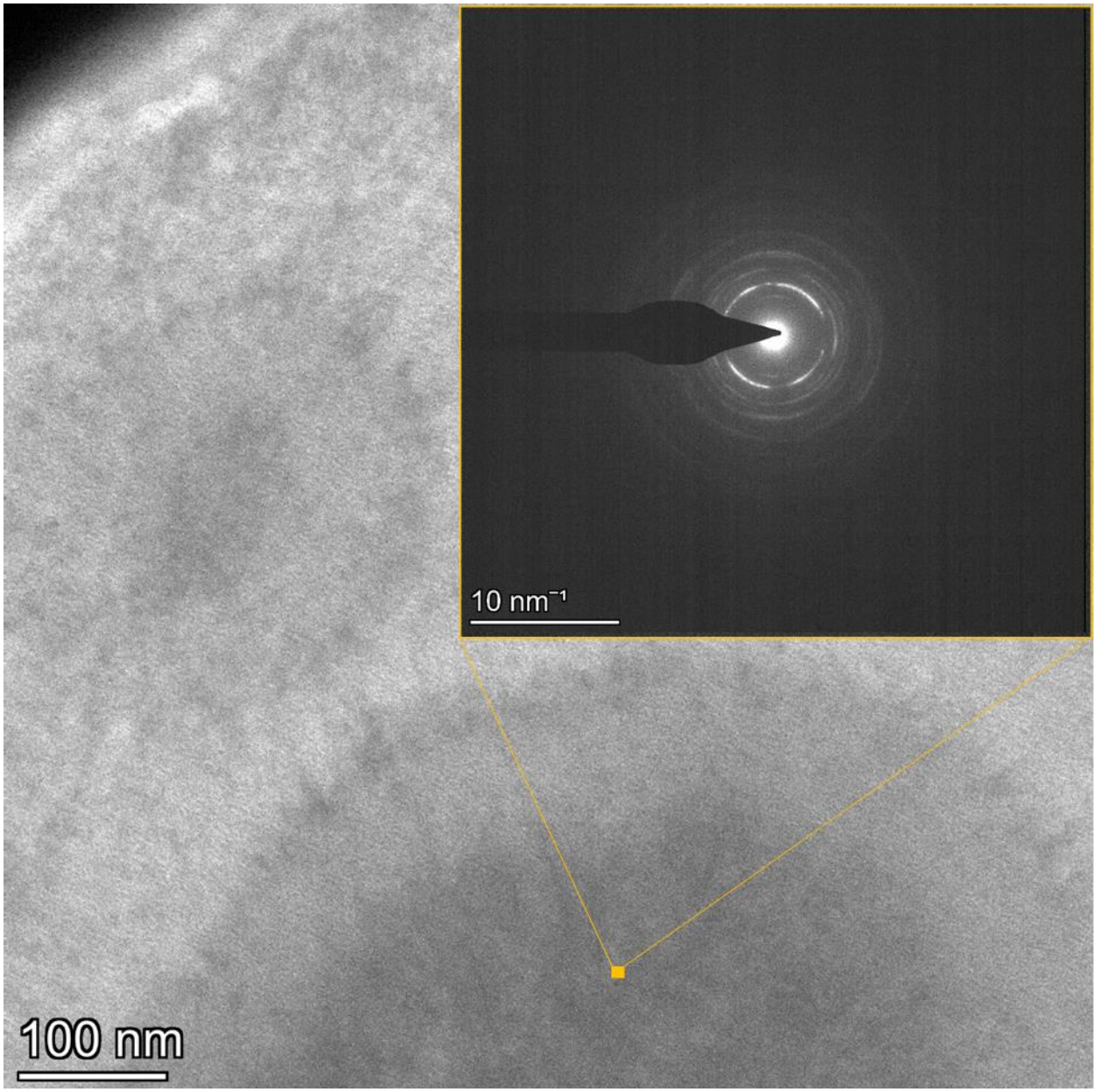

939

940 **Figure S3. Selected-area electron diffraction (SAED) pattern (inset) acquired from the**
941 **core of one of the spheroidal features resulting from E11**. The diffraction geometry is
942 consistent with kutnaharite, based on estimation analyses using AMCSD entry 0001070 (after
943 Peacor et al. 1987).

944

945

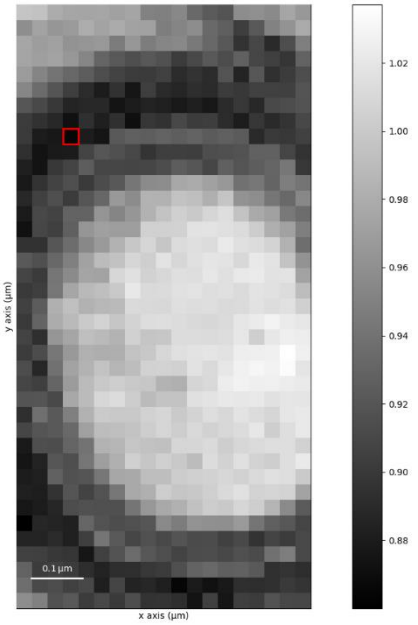

Figure S4. $t(\lambda)^{-1}$ map across a spheroidal ROI. Derived from the low-loss electron energy loss spectra (Malis et al., 1988), the map displays the spatial variation in sample thickness relative to the inelastic mean free path, $t(\lambda)^{-1}$. The darker grey regions correspond to the Mg-rich cortices (e.g., red square), while the bright central regions correspond to the thicker Mn-rich cores ($t(\lambda)^{-1} \approx 1.02$). In this regime ($(\lambda)^{-1} > 0.5$), inelastic scattering significantly contributes to the background signal (unscattered fraction = e^-$t(\lambda)^{-1} \approx 0.41$, i.e., 41% of the beam is coherent (unscattered). The other 59% creates inelastic background noise, which hinders the detection of weak diffraction intensities such as the cation ordering (b-type) superlattice reflections. Calculated using HyperSpy (https://doi.org/10.5281/zenodo.14956374).

Malis, T., Cheng, S. C., & Egerton, R. F. (1988). EELS log-ratio technique for specimen-thickness measurement in the TEM. *Journal of Electron Microscopy Technique*, 8(2), 193–200

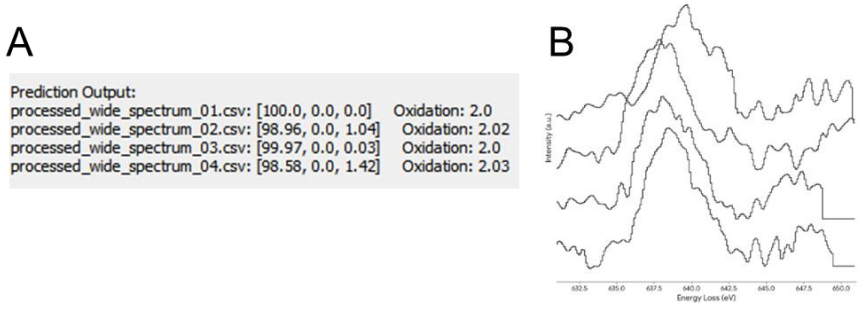

Figure S5. Results of the model MnEdgeNet (https://github.com/xinhuolin/MnEdgeNet/tree/main 5). Stacked raw EELS spectra of the Mn $L_{2,3}$-edge acquired from four representative locations within the spheroid core (range 631–651 eV). Vertical offsets are applied for clarity. All scans consistently display a sharp L_3 absorption maximum at 693.5 to 640.0 eV and a deep inter-peak valley returning to baseline intensity. These identical spectral features confirm the spatial homogeneity of the pure high-spin Mn(II) oxidation state across the analyzed region.

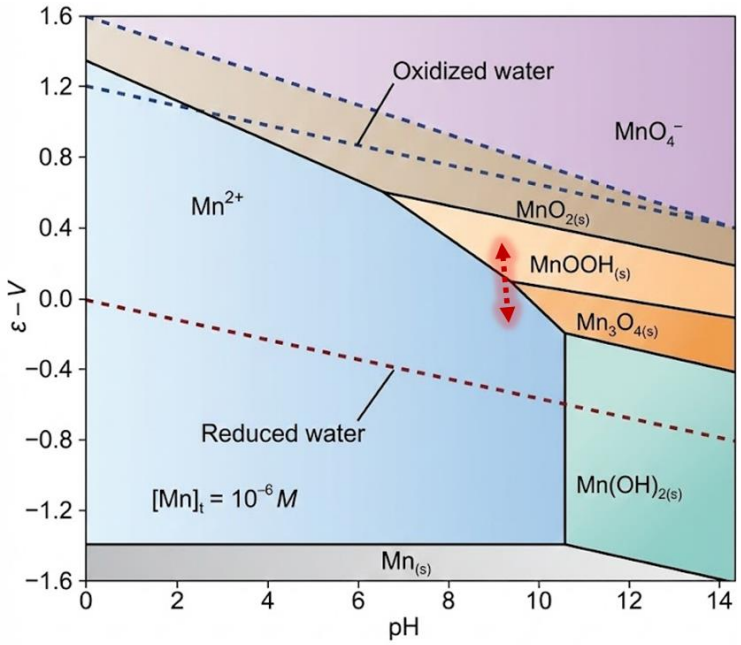

977

978 **Figure S6. Eh-pH stability diagram for the Mn water system at 25°C.** The diagram plots
979 redox potential (ε–V) against acidity (pH), showing the thermodynamically stable fields for
980 various manganese species at a total manganese molar concentration of [Mn]t = 10^{-6} M. Solid
981 lines delimit the stability boundaries between species. Aqueous species shown are the
982 manganous ion (Mn^{2+}) and permanganate (MnO_4^-). Solid phases, denoted by the subscript (s)
983 and distinct color shading, include pyrochroite ($Mn(OH)_2$(s)), hausmannite (Mn_3O_4(s)),
984 manganite (MnOOH(s)), and pyrolusite (MnO_2(s)). Adapted from Faust & Aly (1998) and
985 Stumm & Morgan (1996). The approximate experimental trajectory is shown (arrow)

986

Table S1. Saturation state of relevant mineral phases in the functionalized active electrolyte (E_{11}). Values represent the Saturation Index (SI = log(IAP) - log(K)) calculated for the mixture composition S_{ii}. Positive SI values (>0) indicate supersaturation, while negative values (<0) indicate undersaturation. Note that the S_{ii} is strongly supersaturated with respect to aragonite, dolomite, and hydromagnesite, consistent with the observed mineral assemblage.

Phase	SI	logIAP	logK	Formula
Huntite	8.81	-21.15	-29.97	$CaMg_3(CO_3)_4$
Dolomite	6.09	-11	-17.09	$CaMg(CO_3)_2$
Dolomite(d)	5.54	-11	-16.54	$CaMg(CO_3)_2$
Hydromagnesite	5.01	-3.75	-8.76	$Mg_5(CO_3)_{4(}OH)_2 \cdot 4H_2O$
Rhodochrosite	4.18	-6.95	-11.13	$MnCO_3$
Rhodochrosite(d)	3.44	-6.95	-10.39	$MnCO_3$
Magnesite	2.95	-5.08	-8.03	$MgCO_3$
Calcite	2.55	-5.93	-8.48	$CaCO_3$
Aragonite	2.41	-5.93	-8.34	$CaCO_3$
Artinite	1.88	11.48	9.6	$MgCO_3$:$Mg(OH)_2$:$3H_2O$
Nesquehonite	0.54	-5.09	-5.62	$MgCO_3$:$3H_2O$
Pseudo-kutnahorite†	-2.57	-12.87	-10.3	$MnCa(CO_3)_2$
Nahcolite	-3.12	-3.67	-0.55	$NaHCO_3$
Natron	-5.06	-6.37	-1.31	Na_2CO_3:$10H_2O$
Thermonatrite	-6.47	-6.35	0.12	Na_2CO_3:H_2O
Trona	-9.23	-10.02	-0.8	NaHCO3:Na2CO3:$2H_2O$
Pyrochroite	-0.5	14.7	15.2	$Mn(OH)_2$
Brucite	-0.27	16.57	16.84	$Mg(OH)_2$
Portlandite	-7.08	15.72	22.8	$Ca(OH)_2$
Manganite	-5.11	20.23	25.34	MnOOH
Hausmannite	-5.87	55.16	61.03	Mn_3O4
Bixbyite	-9.96	-10.57	-0.61	Mn_2O_3
$MnCl_2 \cdot 4H_2O$	-7.87	-5.16	2.71	$MnCl_2 \cdot 4H_2O$

Notes: Calculations were performed using the U.S. Geological Survey geochemical code PHREEQC (Parkhurst and Appelo, 2013) employing the wateq4f thermodynamic database. (d) denotes disordered or metastable phases included in the database. † Solubility product (log K_{sp}) for pseudokutnahorite is adapted from Mucci (2004). Data Availability: The input code and full dataset for these calculations are available in the Zenodo repository (see Data Availability Statement).

Supplementary Note S1: Estimation of local interfacial pH and saturation state of dolomite near the electrode-mineral interface

1. Model assumptions

To estimate the magnitude of pH oscillations at the working electrode (WE) surface, we apply a simplified steady-state Nernst-Planck approximation. The model assumes a stagnant diffusion boundary layer (Nernst diffusion layer, Δ) separating the electrode surface from the bulk electrolyte.

We adopt the following governing assumptions:

1. Transport control: mass transport of protons (H^+) and reactants is governed primarily by diffusion across the boundary layer; migration effects are minimized by the supporting electrolyte.
2. Stoichiometry: the anodic oxidation of Mn(II) to Mn(III) coupled with hydrolysis generates protons. We conservatively assume a localized proton flux (J_{H+}) proportional to the measured current density (j).
3. Layer thickness: For an unstirred vertical electrode under natural convection, Δ is estimated at *ca.* 200 μm (2×10^{-2} cm) (Bard & Faulkner, 2001).
4. Bulk conditions: Bulk solution is maintained at pH 9.1 (experimental baseline).

2. Flux Calculation

The J_{H+} generated at the anode is derived from Faraday's Law:

$J_{H+} = j(nF)^{-1}$

Where:

- $j \approx 100$ μA cm^{-2} (T_{peak} current density observed in CV scans).
- n = 1 (electrons transferred per proton equivalent).
- F = 96,485 C mol^{-1} (Faraday constant).

$J_{H+} = 10^{-4}\ (96485) = 1.04 \times 10^{-9}$ mol cm^{-2} s^{-1}

3. Interfacial pH shift

According to Fick's First Law, the concentration gradient (ΔC) required to sustain this flux across layer Δ is:

$$\Delta H^+ \approx J_{H+} \times \delta\ (D_H)^{-1},$$

where:

- $D_H \approx 9.3 \times 10^{-5}$ cm^2 s^{-1} (diffusion coefficient of H^+ in water at 25°C).
- $\delta \approx 0.02$ cm

$\Delta H^+ \approx 1.04 \times 10^{-9}\ (0.02)/(9.3 \times 10^{-5}) \approx 2.21\ 10^{-7}$ M

Resulting surface pH: the bulk proton concentration at pH 9.1 is $[H^+]_{bulk} \approx 7.9 \times 10^{-10}$ M.

The surface concentration $[H^+]_{surf}$ is the sum of the bulk concentration and the anodic accumulation $\Delta[H^+]$):

$$[H^+]_{surf} \approx 7.9 \times 10^{-10} + 2.2 \times 10^{-7} \approx 2.21 \times 10^{-7} \text{ M}$$

$$\underline{pH_{surf} = -\log(2.21 \times 10^{-7}) \approx 6.65}$$

The unbuffered anodic shift is $\Delta pH \approx -2.45$ units. However, in the presence of the (bi)carbonate/alginate buffering system, this theoretical drop can be substantially attenuated (see Fig. 2). Conservatively estimating a 50–70% buffering efficiency, then the effective localized shift is $\Delta pH \approx \pm 0.5$ to 1.2 units.

4. Impact on supersaturation (SI_{dol})

The saturation state for dolomite (SI_{dol}) is defined as:

$$SI_{dol} = \{Ca^{2+}\}\{Mg^{2+}\}\{CO_3^{2-}\}^2 K_{sp}^{-1}$$

Since CO_3^{2-} is strictly pH-dependent, the calculated anodic acidification near the WE surface (pH 9.1 to ~8.0 to 8.5) causes a logarithmic decrease in local carbonate ion activity.

- Anodic phase (oxidation): local pH drops, SI_{dol} decreases significantly (undersaturation or low supersaturation), promoting the dissolution of kinetic defects.
- Cathodic phase (reduction): local pH is restored or increased (via proton consumption), SI_{dol}, driving rapid nucleation.

This confirms that electrochemical cycling imposes a high amplitude oscillation of the saturation state (SI_{dol}), mimicking the Ostwald ripening mechanism required for ordering.

5. Scan rate justification: The electrochemical experiments utilized a fixed scan rate of 10 mV s^{-1}. This rate was selected to establish a stable diffusion profile (δ) that balances the anodic proton production with the buffering capacity of the hydrogel, creating a sustained, reproducible saturation gradient necessary for crystal growth.

References

Bard, A. J., & Faulkner, L. R. (2001). *Electrochemical Methods: Fundamentals and Applications*. Wiley.

Stumm, W., & Morgan, J. J. (1996). *Aquatic Chemistry*. Wiley-Interscience.

Supplementary Note S2. A working-table compiling sedimentary units of interest to test the mechanism proposed in the main text. Have fun.

Period	Formation / Location	Dominant Texture & Key Features	References*
Holocene	Sabkha Flats (Al Jubayl, Saudi Arabia)	Microbial mats; Quaternary ordered dolomite.	(C'hafetz et al., 1999)
Holocene	Sabkha Flats (Abu Dhabi/Qatar)	Microbial mats; protodolomite forming in EPS-rich layers; seasonal cycling.	(Bontognali et al., 2010; Di Loreto et al., 2021)
Holocene	Lake Van (Turkey)	Cyclic early diagenetic dolomite; triggered by hydrochemical mixing and redox perturbations.	(McCormack et al., 2018, 2024)
Miocene	Eger Rift Paleolake (Czech Rep.)	Episodic carbonate cementation driven by Mn–N redox cycling in a non-marine setting.	(Petrash et al., 2025)
Eocene	Green River Formation (USA)	Lacustrine dolomite; vast deposits formed in organic-rich, stratified (meromictic) alkaline paleolakes.	(Pommer et al., 2023)
Triassic (Ladinian)	Dolomite Mtns / Sella Group (Italy)	The "Dolomite" Archetype. synsedimentary	Meister et al., 2013), Sedimentology 60(1):270-291
Permian-Triassic	Inner Platform (Dinarides, Croatia)	Dolomitization linked to oceanic anoxia and chemocline shifts; inner platform facies.	(Aljinović et al., 2025)
Devonian	Ratner Formation (Canada, SK)	Partially recrystallized medium-sized dolomite with high. Mn contents (ME)	Fu & Qinq, 2010, *Carbonates and Evaporites* 26, 111-115
Devonian	Grosmont Formation (Canada, AB)	Sabkha dolomite forming within burrowed stromatolites; microbial influence.	(Baniak et al., 2014)
Upper Cambrian (Furongian)	Chaomidian Fm. (North China Platform)	Fabric-retentive microbial dolomite; thrombolite-stromatolite reefs	(Han et al., 2024; Chen et al., 2014)

Period	Formation / Location	Dominant Texture & Key Features	References*
Lower Cambrian	Xiaoerbulake Fm. (Tarim Basin, China)	Fabric-retentive dolomicrite; microbialites (stromatolites/thrombolites).	(Zhang et al., 2022; Zheng et al., 2022)
Ediacaran (Shuram Excursion)	Khufai, Buah & Birba Fms (Oman)	Primary Nanoscale Fabrics; fibrous dolomite ooids, spherulitic stromatolites, and fibrous cements.	(Wilcots et al., 2025)
Ediacaran	Doushantuo Formation (China)	Cap dolostone featuring interlinked cycles of methane, manganese, and sulfate.	(Cai et al., 2023)
Mesoproterozoic (~1.6 Ga)	McArthur Basin (Amelia/Mara Dol.), Australia	Massive fabric-retentive dolostone; Mn-mineralized sheaths; exceptional eukaryotic cell preservation.	(Muir, 1976, 1983)
Mesoproterozoic (~1.6 Ga)	Chuanlinggou Formation, N China	Fabric retentive. Mn-bearing dolomitic siltstone	(Xu et al., 2025)
Mesoproterozoic (~1.5 Ga)	Gaoyuzhuang Formation, N China	Syndiagenetic, consist of dolommicrite, along with kutnohorite and rhodochrosite	(Xu et al., 2025)
Mesoproterozoic (~1.4–1.1 Ga)	Bangemall Supergroup (W. Australia)	Sizable Mn deposits associated with surface oxygenation events.	(Spinks et al., 2023)
Paleoproterozoic (~2.1 Ga)	Francevillian Succession (Gabon)	Intimate association Mn-Ca carbonate	(Nzamba et al., 2026; Préat et al., 2011)

1067 * (Refer to the main text). Unless otherwise indicated.